Graphical impedance-matching method for a superconducting parametric amplifier

Kaiyong He,[1,*] Qing Yu,[1] Liangliang Yang,[1] Yongcheng He,[1] Jianshe Liu,[1] and Wei Chen[1,2,3,†]

[1] *Laboratory of Superconducting Quantum Information Processing, School of Integrated Circuits, Tsinghua University, 100084 Beijing, China*

[2] *Beijing National Research Center for Information Science and Technology, 100084 Beijing, China*

[3] *Beijing Innovation Center for Future Chips, Tsinghua University, 100084 Beijing, China*

(Received 6 September 2023; revised 6 December 2023; accepted 1 March 2024; published 26 March 2024)

This work proposes a graphical impedance-matching method for superconducting parametric amplifiers with quantum-limited noise performance using a modified Smith chart. It enables one to quickly apply the impedance-matching methods in microwave engineering to the design of parametric amplifiers. When the matching networks are composed of resonators and their equivalents, the matching of a parametric amplifier can be reduced to that of a negative-resistance amplifier, which is generally invalid due to the connection between the signal-frequency and idler-frequency networks introduced by the parametrically modulated component. Several examples are presented to demonstrate the effective and efficient matching of parametric amplifiers using this method, circumventing the need for complex calculations. This method also offers intuitive insight into how variations in pump strength and bias affect the amplification behavior of the circuit, which is useful in characterizing the parametric amplifier and finding the optimal operating state.

DOI: 10.1103/PhysRevApplied.21.034055

I. INTRODUCTION

Quantum-limited amplification and precise detection of weak microwave signals are of central significance in superconducting quantum information processing due to the constraints imposed by quantum systems on the allowed probe power level [1–4]. In circuit quantum electrodynamics, they are generally realized by superconducting parametric amplifiers (SPAs), which provide high gain and quantum-limited noise performance [5–16]. In large superconducting quantum processors, frequency-domain multiplexing for readout of multiple qubits is used. It requires that SPAs should also have high saturation powers and large bandwidths [17].

This work focuses on the negative-resistance reflection SPA, of which a Josephson parametric amplifier (JPA) serves as a typical example [5,7]. Compared with other SPAs, it has higher quantum efficiency, while being easy to prepare. By having superconducting-quantum-interference-device (SQUID) arrays as nonlinear elements, it achieves a high saturation power [18–21]. Broadening the bandwidth of a JPA is generally realized by the impedance-matching method, which has been experimentally realized. Impedance matching the JPA with a Klopfenstein taper is an effective method to achieve a large bandwidth [19,22–25]. However, its design principle is vague. Bandwidth can also be increased by engineering the imaginary part of the environmental impedance [26–30]. The method is based on equations of motion of a JPA, offering a clear explanation of how broadband is achieved. The network-synthesis method is a more-general analytical approach for broadband-amplifier design [31–36]. It proved that engineering the imaginary part of the environmental impedance introduced in Ref. [26] is equivalent to synthesizing a two-pole max-flat (Butterworth) matching network. Broadband amplifiers have also been investigated with use of Chebyshev and Legendre prototypes for matching [18,37].

This work proposes a graphical method based on the modified Smith chart for impedance matching of a parametric amplifier (PA). It does not require complicated calculation for specific cases, increasing the efficiency of impedance matching, and meanwhile it is able to provide impedance-matching networks that are challenging to deduce analytically from other approaches. The conventional Smith chart is an efficient and intuitive tool for impedance matching in microwave engineering [38,39], but its direct application to PA matching presents challenges. One major hurdle lies in the negative-resistance characteristic inherent to PAs, which are therefore usually described with use of negative-resistance models [40,41].

*heky19@mails.tsinghua.edu.cn

†weichen@tsinghua.edu.cn

The conventional Smith chart is inconvenient for representing negative resistance. To address this, we have introduced a modification that makes it suitable for representing negative-resistance circuits, especially negative-resistance amplifiers (NRAs). The second difficulty arises from the fact that the parametric amplifier is not simply equivalent to an ideal NRA, because its parametrically modulated component connects the signal-frequency and idler-frequency matching networks, resulting in more-complex behavior. However, we identify a situation where a connection is established between the two. Specifically, this connection occurs when the matching network is composed of resonators or their equivalent components. In this case, matching a PA is equivalent to matching an NRA. This method bridges the gap between conventional matching techniques in microwave engineering and those for PAs, allowing quick application of the techniques to PA matching. This method also serves as a valuable tool for characterizing PAs and finding optimal operating states. In this paper, several impedance-matching examples for a JPA are shown, but the method is also suitable for other types of PA.

II. SIGNAL-IDLER INTERACTION OF A SUPERCONDUCTING PARAMETRIC AMPLIFIER

Parametric amplification circuits contain components that are parametrically modulated by the pump tone. Energy is transferred from the pump tone to the input tone, leading to amplification [2,42]. While early implementations used varactors, which are modulated capacitors, in a microwave circuit [35], modern amplifiers commonly use parametrically modulated inductors. In practice, these inductors are realized by superconducting components, such as superconducting films with appreciable kinetic inductance [16,43], Josephson junctions, and SQUIDs (see Appendix A) [22,26]. Without loss of generality, this paper focuses the discussion on a sinusoidally modulated inductor, and the results can be extended to other parametric amplification systems.

Consider a parametrically modulated inductor that is time dependent:

$$\begin{aligned} L(t) &= L_0 + 2L_1\cos(\omega_p t - \phi_p) \\ &= L_0 + (\delta L e^{-i\omega_p t} + \delta L^\star e^{i\omega_p t}), \end{aligned} \tag{1}$$

where L_0 is the constant inductance, $\delta L = L_1\exp(i\phi_p)$ is the complex modulated amplitude, ω_p is the pump frequency, and the factor 2 is introduced for convenience.

The inductor is, in general, shunted by a capacitor C_0, forming a pumped resonator whose Hamiltonian is given by

$$\hat{H}_{sys} = \frac{1}{2}C_0[\hat{V}(t)]^2 + \frac{1}{2}L_0[\hat{I}(t)]^2\left[1 + (\alpha e^{-i\omega_p t} + \alpha^\star e^{i\omega_p t})\right], \tag{2}$$

where $\alpha = \delta L/L_0$ is the ratio of the modulated inductance to the constant inductance, representing the effective pumping strength. With use of the transformation

$$\hat{a}(t) = \frac{1}{\sqrt{2\hbar Z_c}}L_0\hat{I}(t) + i\sqrt{\frac{Z_c}{2\hbar}}C_0\hat{V}(t), \tag{3}$$

the Hamiltonian becomes

$$\hat{H}_{sys} = \hbar\omega_0[\hat{a}^\dagger(t)\hat{a}(t) + (\alpha e^{-i\omega_p t} + \alpha^\star e^{i\omega_p t})(\hat{a}(t) + \hat{a}^\dagger(t))^2], \tag{4}$$

where $\hat{a}(t)$ is the annihilation operator of the resonator and $[\hat{a}(t), \hat{a}^\dagger(t)] = 1$. $Z_c = \sqrt{L_0/C_0}$ is the characteristic impedance of the resonator, $\omega_0 = 1/\sqrt{L_0C_0}$ is the resonant frequency, and the constant energy is omitted in Eq. (4).

With use of the Heisenberg equation, and with incorporation of effects of the port to which the system is coupled, the resonator's equation of motion is

$$\begin{aligned} \frac{d\hat{a}(t)}{dt} &= \left(-i\omega_0 - \frac{\kappa}{2}\right)\hat{a}(t) - 2i\omega_0\left(\alpha e^{-i\omega_p t} + \alpha^\star e^{i\omega_p t}\right) \\ &\quad\times\left[\hat{a}(t) + \hat{a}^\dagger(t)\right] + \sqrt{\kappa}\hat{a}_{in}(t), \end{aligned} \tag{5}$$

where κ is the dissipation rate introduced by the coupling to the signal port and $\hat{a}_{in}(t)$ is the "input mode" (see Appendix B).

Transformation of Eq. (5) to the frequency domain yields the system susceptibility matrix $\chi(\omega_s)$, which relates the intracavity fields $\vec{a} = [\hat{a}(\omega_s), \hat{a}^\dagger(\omega_i)]^T$ to the input fields $\vec{a}_{in} = [\hat{a}_{in}(\omega_s), \hat{a}^\dagger_{in}(\omega_i)]^T$ as $\vec{a} = \chi(\omega_s)\sqrt{\kappa}\vec{a}_{in}$, where

$$[\chi(\omega_s)]^{-1} = -i\begin{bmatrix} \omega_s - \omega_0 + i\kappa/2 & -2\omega_0\alpha \\ 2\omega_0\alpha^\star & -\omega_i + \omega_0 + i\kappa/2 \end{bmatrix}, \tag{6}$$

where $\omega_s = \omega_p/2 + \delta\omega$ is the signal frequency, $\omega_i = \omega_p/2 - \delta\omega$ is the idler frequency, and evidently $\omega_p = \omega_s + \omega_i$, indicating that it is a frequency-mixing process. The boundary condition that connects the input field $\vec{a}_{in}$ and the output field $\vec{a}_{out} = [\hat{a}_{out}(\omega_s), \hat{a}^\dagger_{out}(\omega_i)]^T$ is $\vec{a}_{in} + \vec{a}_{out} = \sqrt{\kappa}\vec{a}$, and it leads to the generalized scattering matrix of the system:

$$S = \kappa\chi(\omega_s) - \mathbb{I}, \tag{7}$$

where $\mathbb{I}$ is a 2×2 identity matrix and $\vec{a}_{out} = S\vec{a}_{in}$. S_{11} is the signal amplitude gain and S_{21} is the intermodulation amplitude gain between the signal mode and the idler mode.

A more-general perspective for the shunt capacitor C_0 is to regard it as part of the matching network between the parametrically modulated inductor and the input port

with characteristic impedance Z_s, as shown in Fig. 1(a). This perspective will allow one to capture the feature of the single parametrically modulated component and offer an understanding of the roles of the physical matching network for both the signal frequency and the idler frequency and the way they interact with each other. The voltage operator $\hat{V}(t)$ and the current voltage operator $\hat{I}(t)$ are used to illustrate the perspective, and they are connected to the canonical mode $\hat{a}(t)$ by Eq. (3).

When the current $\hat{I}(t)$ flowing through the inductor is composed of two frequency components

$$\hat{I}(t) = \sum_{k=\mathrm{s,\,i}} \frac{\hat{I}_k e^{j\omega_k t} + \hat{I}_k^\dagger e^{-j\omega_k t}}{2}, \tag{8}$$

where $\omega_k \neq \omega_p$, the voltages at ω_s and ω_i across the inductor are

$$\begin{aligned} \hat{V}_s &= j\omega_s L_0 \hat{I}_s + j\omega_s \delta L \hat{I}_i^\dagger, \\ \hat{V}_i^\dagger &= -j\omega_i \delta L^\star \hat{I}_s - j\omega_i L_0 \hat{I}_i^\dagger. \end{aligned} \tag{9}$$

Here, the voltage is derived from $\hat{V}(t) = \mathrm{d}[L(t)\hat{I}(t)]/\mathrm{d}t$. The voltages at frequencies other than ω_s and ω_i are assumed to be shorted out, which is a form of the rotating-wave approximation in the physical view. $j \equiv -i$ is used to ensure agreement with the usual electrical engineering sign convention. The voltage $\hat{V}_s$ at ω_s is related to the current at the other frequency ω_i, and the voltage $\hat{V}_i^\dagger$ at ω_i is related to the current at ω_s. This means that frequency mixing occurs, and the two components are coupled. When $\omega_s = \omega_i$, the device works in the degenerate mode, and when $\omega_s \neq \omega_i$, it works in the nondegenerate mode.

From Eq. (9), the impedance matrix of the modulated inductor is given by

$$Z = \begin{bmatrix} jX_{11} & jX_{12} \\ j(-X_{21}) & j(-X_{22}) \end{bmatrix}, \tag{10}$$

where

$$\begin{cases} X_{11} = \omega_s L_0, & X_{12} = \omega_s \delta L, \\ X_{21} = \omega_i \delta L^\star, & X_{22} = \omega_i L_0. \end{cases} \tag{11}$$

By transformation using the *ABCD* matrix (see Appendix C), the modulated inductor can be factored into three parts in series, as shown is Fig. 1(b). The constant inductance in Eq. (1) serves as two series constant inductors at ω_s and ω_i, and the parametrically modulated term works as a generalized impedance inverter [31,44,45]. The matching network and the reference impedance Z_s in Fig. 1(a) appear twice at both the signal frequency and the idler frequency. Components on the left of the inverter are for the signal frequency ω_s and the mirrored components on the right are for the idler frequency ω_i. The input impedance $Z_1(\omega_s)$ seen from the inverter at the signal frequency is related to that at the idler frequency:

$$Z_1(\omega_s) = -\frac{X_{12}X_{21}}{Z_1'(\omega_i)} = -\frac{\eta(\omega_s,\omega_i)}{Z_1'(\omega_i)}, \tag{12}$$

where

$$\eta(\omega_s,\omega_i) = \omega_s\omega_i |L_0|^2 |\alpha|^2 \tag{13}$$

is the conversion coefficient. For $Z_1'(\omega_i)$ with a positive real part, i.e., $\mathrm{Re}[Z_1'(\omega_i)] > 0$, there is $\mathrm{Re}[Z_1(\omega_s)] < 0$, a negative resistance resulting in signal amplification. This is how a PA is to be regarded as an NRA. When the matching network is lossless, $\mathrm{Re}[Z_1(\omega_s)] = -\eta(\omega_s,\omega_i)/Z_s$, which means that the negative resistance is dependent on the reference impedance Z_s.

The admittance matrix of the modulated inductor is easily derived from the impedance matrix Z [44]:

$$Y = \begin{bmatrix} j(-B_{11}) & j(-B_{12}) \\ jB_{21} & jB_{22} \end{bmatrix}, \tag{14}$$

where

$$\begin{cases} B_{11} = \frac{1}{\omega_s L_0^\alpha}, & B_{12} = \frac{\alpha}{\omega_i L_0^\alpha}, \\ B_{21} = \frac{\alpha^\star}{\omega_s L_0^\alpha}, & B_{22} = \frac{1}{\omega_i L_0^\alpha}, \end{cases} \tag{15}$$

where $L_0^\alpha = L_0(1-|\alpha|^2)$. The parametrically modulated inductor is again factored into three parts by use of the *ABCD* matrix, and the three parts are in parallel here, as shown in Fig. 1(c). This is equivalent to a generalized admittance inverter sandwiched by two parallel constant inductors.

The input admittance $Y_1(\omega_s)$ seen from the generalized admittance inverter at the signal frequency is given by

$$Y_1(\omega_s) = -\frac{B_{12}B_{21}}{Y_1'(\omega_i)} = -\frac{\eta^\alpha(\omega_s,\omega_i)}{Y_1'(\omega_i)}, \tag{16}$$

where

$$\eta^\alpha(\omega_s,\omega_i) = \frac{|\alpha|^2}{\omega_s\omega_i L_0^{\alpha 2}}. \tag{17}$$

Similarly, the modulated inductor converts a positive conductance at the idler frequency to a negative conductance at the signal frequency. $\eta(\omega_s,\omega_i)$ and $\eta^\alpha(\omega_s,\omega_i)$ are some functions of the frequencies ω_s and ω_i. Later in this paper, for simplicity, their values at the center of the frequency band are used, denoted as η and η^α. With the simplicity, the graphical impedance-matching method is suitable for the designs whose fractional bandwidths are up to approximately 20%. Because of the nonlinearity of the

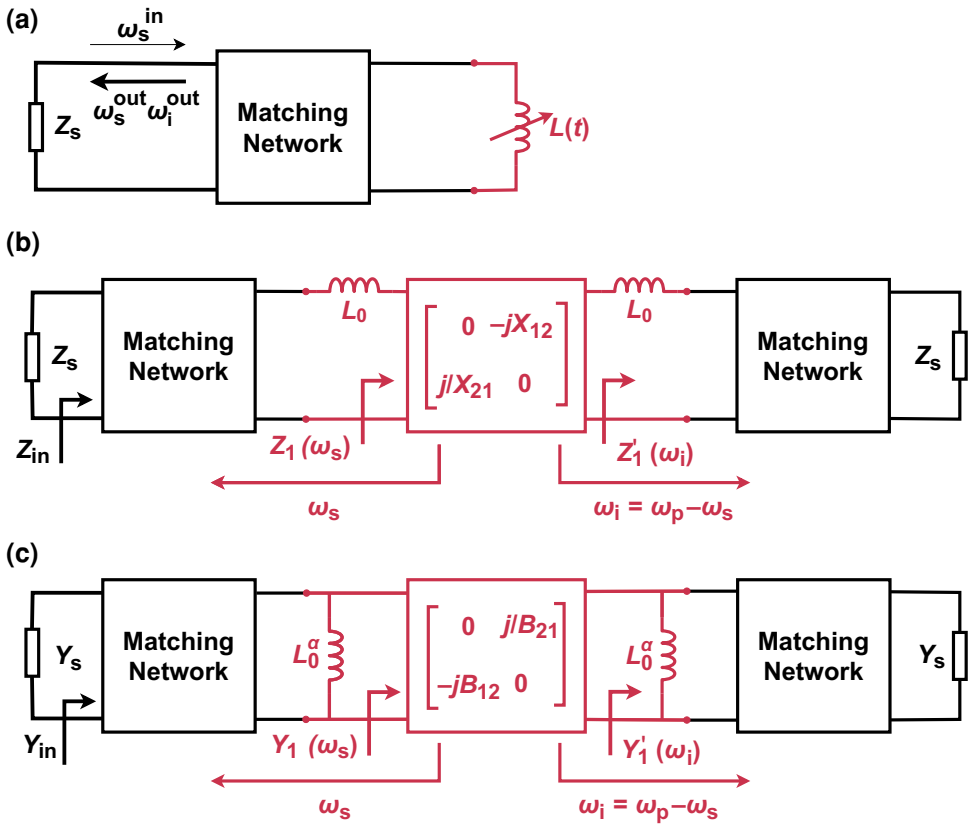

FIG. 1. PA with a matching network. (a) Circuit diagram of a PA with a matching network. (b) Equivalent-circuit model for the series representation of the PA. The networks at signal and idler frequencies are coupled by a generalized impedance inverter. (c) Equivalent-circuit model for the parallel representation of the PA. The networks at signal and idler frequencies are coupled by a generalized admittance inverter.

superconducting components, the actual behavior of the device at high gain may deviate from the predictions of the method. Consequently, for a single-stage amplifier, a reasonable gain obtained with this method should be below 40 dB.

When the effect of the matching network is taken into account, the *ABCD* matrix of the entire circuit can be derived. By specifying the reference impedance of the port, one can transform the *ABCD* matrix to obtain the generalized scattering matrix that connects $\vec{V}^{out}$ and $\vec{V}^{in}$: $\vec{V}^{out} = S\vec{V}^{in}$ [44], where $\vec{V}^{out} = \left[\hat{V}_s^{out}, \hat{V}_i^{\dagger out}\right]$ and $\vec{V}^{in} = \left[\hat{V}_s^{in}, \hat{V}_i^{\dagger in}\right]$. In this case, S_{11} is the signal amplitude gain and S_{21} is the intermodulation amplitude gain. When the matching network is a capacitor, an *LC* resonator is formed with the parametrically modulated inductor. If one takes the Manley-Rowe relations into account, this scattering matrix is consistent with that obtained from Eqs. (6) and (7) [31,46]. The dissipation rate κ is associated with the port impedance Z_s. In the series representation, $\kappa = Z_s/L_0$, while in the parallel representation, $\kappa = 1/Z_s C_0$.

III. GRAPHICAL REPRESENTATION FOR IMPEDANCE MATCHING

Before discussing specific PAs, we first consider the reflective NRA, which is a general model used for the description of a PA [2,40,41]. Equation (12) shows that the parametrically modulated component is related to the negative resistance. The gain of an NRA can be derived from its reflection coefficient $G = |S_{11}|^2 = |\Gamma_G|^2$, where

$$\Gamma_G = \frac{(-R_{PA} + jX_{PA}) - Z_s}{(-R_{PA} + jX_{PA}) + Z_s}. \tag{18}$$

Here $-R_{PA}$ is the negative input resistance seen from the port and X_{PA} is the corresponding input reactance. For convenience, R_{PA} is chosen to be positive and real. Equation (18) is a Möbius transformation connecting the input impedance with the reflection coefficient. One conventional graphical representation of the relationship is the widely used Smith chart, with which microwave engineers are familiar (see Appendix D) [44]. In general microwave circuits, use of the Smith chart for impedance matching proves convenient and practical. In addition, displaying measurement results in the Smith chart helps capture various device characteristics. Nevertheless, accommodating circuits with negative resistance necessitates an expansion of the families of circles that make up the conventional Smith chart, rendering it considerably impractical and infeasible for NRAs.

This work introduces a modification of the conventional Smith chart, aiming to enable its use for a negative-resistance circuit with the minimal alteration. Note that Eq.

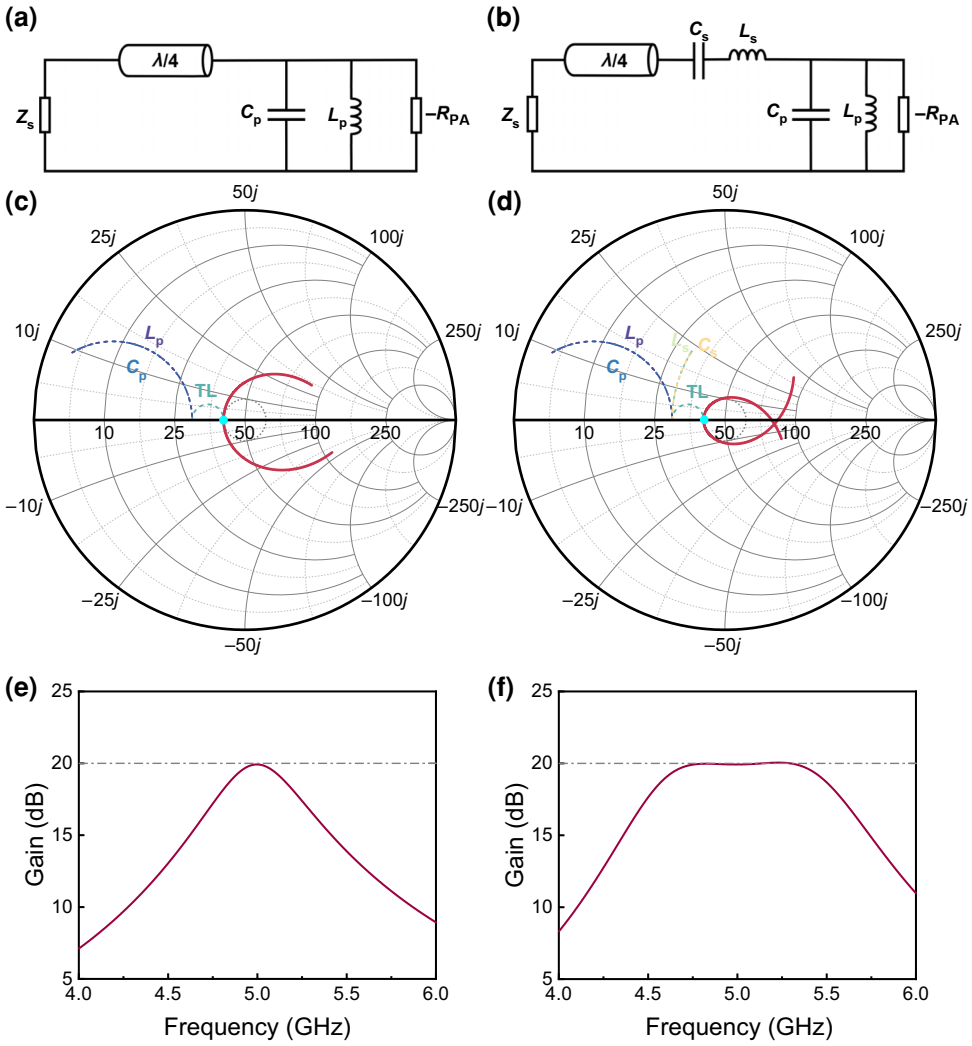

FIG. 2. Illustrative examples of the graphical representation for matching an NRA. (a) Matching of a narrowband NRA. (b) Matching of a broadband NRA. (c),(d) Gain of the narrowband NRA and the broadband NRA, respectively, represented in modified Smith charts. The solid red lines are the gain curves. The dashed lines are the matching paths of each component. The dotted circle in the center of the chart refers to the constant gain circle of 20 dB. (e),(f) Gain profiles of the narrowband NRA and the broadband NRA, respectively. TL, transmission line.

(18) can be rewritten as

$$\Gamma_G = \left(\frac{R_{PA} - jX_{PA} - Z_s}{R_{PA} - jX_{PA} + Z_s}\right)^{-1} = \frac{1}{|\Gamma_p|} e^{j\varphi_p}, \tag{19}$$

where

$$|\Gamma_p| e^{j\varphi_p} = \frac{R_{PA} + jX_{PA} - Z_s}{R_{PA} + jX_{PA} + Z_s}. \tag{20}$$

It implies that the reflection coefficient of a negative-resistance circuit can be expressed with use of its positive-resistance counterpart. The key consideration lies in recognizing that the voltage gain is the reciprocal of the reflection coefficient of the positive-resistance circuit, with the phase remaining unaffected. With this approach, several widely used effective matching methods based on the Smith chart can be directly applied to match an NRA.

Figure 2 presents illustrative examples showing the matching of reflection NRAs. In Fig. 2(a), R_{PA} is 30 Ω. The presence of a constant shunt inductor $L_p = 338$ pH constrains the frequency response of the amplifier. Typically, this inductance is resonated out with use of a parallel capacitor C_p, which is selected to have a capacitance of 3 pF here, establishing a resonator with a central frequency of 5 GHz. To match the input impedance to the port's reference impedance, which is, in general, $Z_s = 50$ Ω, a $\lambda/4$ transmission line is used. In the context of a positive-resistance circuit, the reflection coefficient is zero when the input impedance is perfectly matched, i.e., $Z_{in} = 50$ Ω. For its negative-resistance counterpart, this means that

the gain is infinite. However, practical constraints prevent realization of infinite gain. When the gain of an NRA is excessively high, higher-order nonlinear effects come into play, imposing limitations on the achievable gain. Consequently, aiming for a gain that is too high does not make sense. Generally, an appropriate resistance value is selected to achieve a desired gain level. For instance, when aiming for a target gain of 20 dB, one can opt to transform the input impedance to 40.9 Ω rather than 50 Ω. The corresponding characteristic impedance of the $\lambda/4$ transmission line is 35 Ω.

Figure 2(c) shows the implementation of the matching process in a modified Smith chart. The dashed lines depict the matching paths of each component, which are consistent with those in the conventional Smith chart [39]. A notable departure from the conventional chart is the representation of the gain curve depicted by the solid red line, which corresponds to a reflection coefficient greater than 1, as given in Eq. (19). The cyan dot indicates a central gain of 20 dB at the resonant frequency, and the gain profile of this circuit is shown in Fig. 2(e), displaying a Lorentzian shape.

The gain curve in Fig. 2(c) is tangent to the dotted circle, which is the voltage-standing-wave-ratio (VSWR) circle used to assist matching of positive-resistance circuits in conventional Smith charts, where VSWR is, $\mathscr{R}_{\rm SW} = (1+|\Gamma|)/(1-|\Gamma|)$. However, what it represents here is the constant-gain circle, serving as a visual reference in the design of NRAs. The objective is not to confine the gain curve within the circle as in the design of positive-resistance circuits, but is rather to fit the curve as closely as possible to the circle in a wide bandwidth. The broader the portion of the curve that fits the circle, the larger the bandwidth. This concept is exemplified by the circuit shown in Fig. 2(b), where a series resonator is added, and $L_{\rm s} = 725$ pH, while $C_{\rm s} = 1.4$ pF. Figure 2(d) shows its gain curve in the modified Smith chart, which fits the constant-gain circle better. In Fig. 2(f), a broad and flat gain profile is shown, where the gain is 20 dB in a large bandwidth. The series resonator does not influence the input impedance at the central frequency but affects the slope of its imaginary part. Consequently, in the modified Smith chart, the position of the central frequency does not move, and other frequency points converge to the constant-gain circle, as shown in the change from Fig. 2(c) to Fig. 2(d). This matching procedure is easily performed by tuning the components using a Smith-chart software program (for example, SimSmith [47] or SMITH [48]), without the need for intricate calculations.

IV. MATCHING OF PARAMETRIC AMPLIFIERS

As previously indicated, under appropriate pumping, a parametrically modulated component has the ability to convert a positive impedance at the idler frequency into a negative impedance at the signal frequency. Consequently, it is often studied with use of a negative-resistance model. However, this does not imply that a PA is equivalent to an NRA, which was described in the preceding sections. There are notable distinctions between them, particularly in terms of impedance matching. The matching technique used for NRAs is valid only within certain specific scenarios.

When one is matching a PA, a pivotal characteristic emerges: the matching components impact the signal-frequency and the idler-frequency matching networks simultaneously, a consideration absent in the case of matching an NRA. This attribute is elucidated through the example of a PA depicted in Fig. 3(a), where a modulated inductor is used. A series capacitor is inserted between the inductor and the reference port to be the matching network. (Note that this capacitor serves only to illustrate the impact of incorporating a component in the matching network of a PA, and does not imply that the circuit has been suitably matched to operate effectively at this stage.) With use of the generalized admittance inverter model of the modulated inductor shown in Fig. 1(c), the circuit evolves into the arrangement depicted in Fig. 3(b). It is evident that when a physical component is introduced into the circuit as part of the matching network, the component's influence

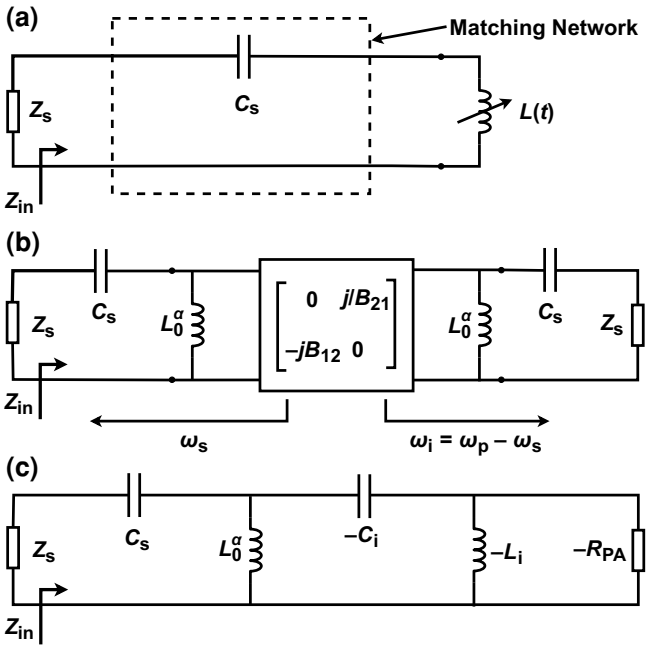

FIG. 3. Matching of a PA and the equivalent negative-resistance circuit. (a) Matching a parametrically modulated inductor with a series capacitor. (b) Equivalent-circuit model with the generalized admittance inverter. The series capacitor appears in both the signal-frequency network and the idler-frequency network. (c) Equivalent negative-resistance model of the PA. The inverter and the subsequent elements at the idler frequency are replaced by their dual counterparts.

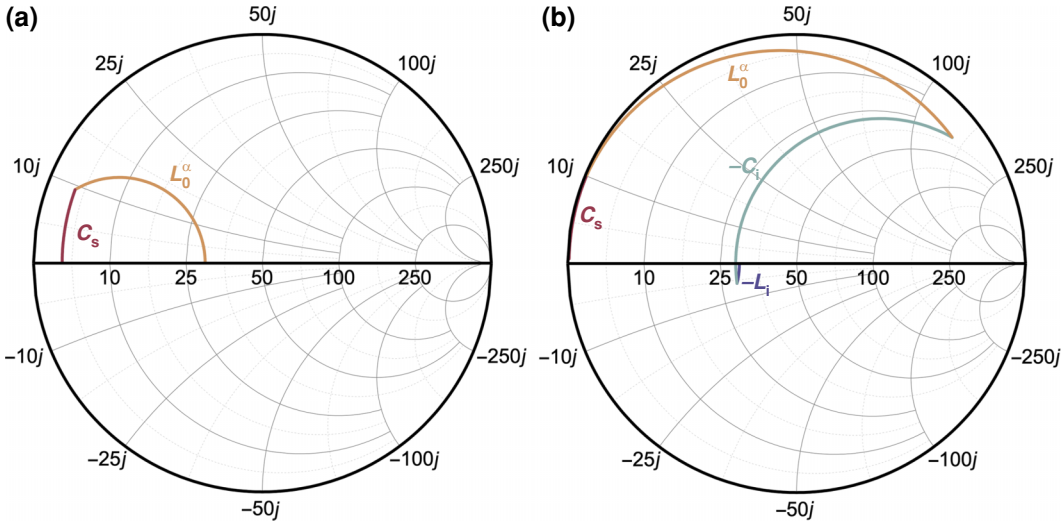

FIG. 4. Matching paths of a PA. (a) Matching paths of the one-stage physical L network. (b) Matching paths of the equivalent cascaded two-stage L network. The mirrored L network is composed of negative inductance $-L_i$ and negative capacitance $-C_i$.

not only appears in the signal-frequency network but also manifests itself symmetrically in the idler-frequency network. It impacts twice the input impedance Z_{in} seen from the reference port at the signal frequency, and thus the gain.

In Fig. 3(c), the equivalent negative-resistance model of this PA is presented, wherein the inverter and its subsequent components have been replaced by their dual counterparts. The parallel inductor L_0^α and series capacitor C_s in the idler-frequency network are, respectively, replaced by the negative series capacitor $-C_i$ and the negative parallel inductor $-L_i$, with their values scaled by the conversion coefficient, i.e., $-C_i = -L_0^\alpha \eta^\alpha$ and $-L_i = -C_s/\eta^\alpha$. The dual negative resistance $-R_{PA}$ is $-1/Z_s\eta^\alpha$. When a physical L network (C_s and L_0^α here) is used for matching—an approach often used in conventional microwave circuits [49,50]—a cascaded two-stage L network emerges in the equivalent negative-resistance circuit.

Figures 4(a) and 4(b) illustrate the results of the matching of an NRA using only the one-stage physical L network and the corresponding cascaded two-stage L networks, respectively, where Z_s is 50 Ω, $-R_{PA}$ is −30 Ω, L_0^α is 338 pH, and C_s is 3.4 pF. Evidently, these results differ. The greater the number of components that are added to the physical matching networks, the greater the effect the mirror components will have on the results, making the matching process less clear. Consequently, achieving a successful match for a PA necessitates more-careful and more-skillful considerations.

However, there exists a scenario where matching a PA can be equated to the matching of an NRA, where each component in the matching network contributes explicitly to the gain only once. This is when the matching network is composed of resonators. Figure 5 shows such a matching network, in which series and parallel resonators appear alternately. In this case, the matching method based on the modified Smith chart presented in Sec. III can be effectively applied to the matching of a PA.

The equivalence of the matching of a PA and the matching of an NRA comes from the correlation of the signal and idler modes [51,52]. The signal amplitude gain S_{11} and the intermodulation gain S_{21} satisfy the relation (see Appendix E)

$$|S_{11}|^2 = |S_{21}|^2 + 1. \tag{21}$$

The total reflected power gain of the amplifier G_P is about 4 times the power gain at the signal frequency $G_{PA} = |S_{11}|^2$ when it is large enough:

$$G_P = (|S_{11}| + |S_{21}|)^2 \simeq 4G_{PA}. \tag{22}$$

This relation can be directly derived from the susceptibility matrix $\chi(\omega_s)$ and the scattering matix, which given by Eqs. (6) and (7), and their generalized form [31,51,53]. In the following, from the lumped-circuit approach, it will be evident that G_P is actually the gain of the NRA G_{NRA}, demonstrating the equivalence in matching between a PA and an NRA.

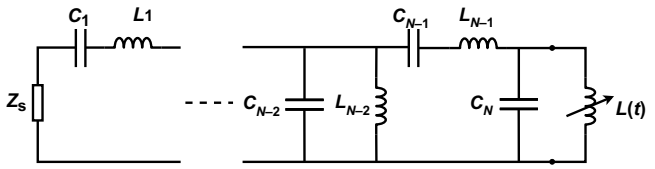

FIG. 5. PA with a matching network composed of resonators.

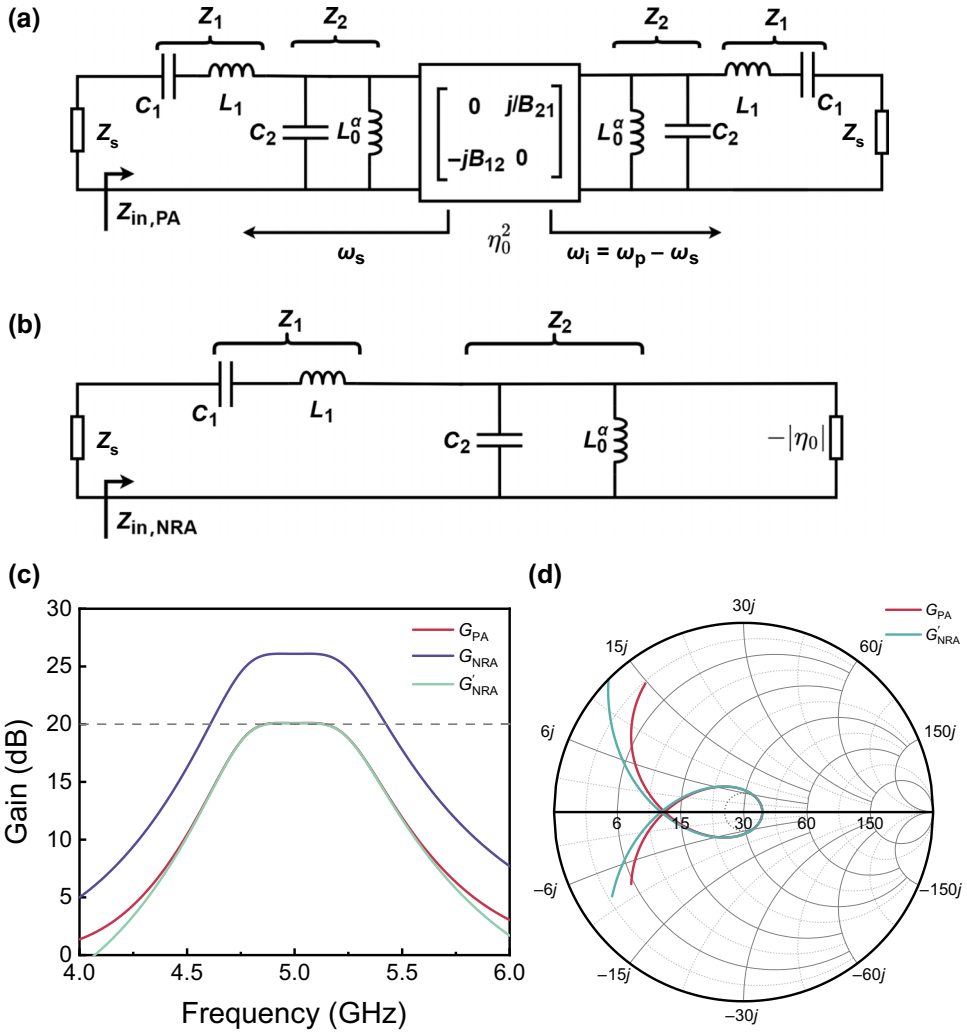

FIG. 6. Equivalence of a PA and an NRA with the matching network composed of resonators. (a) Equivalent-circuit model for the parallel representation of a PA with conversion coefficient η_0^2. (b) Equivalent NRA model of a PA with a negative load $-|\eta_0|$. (c) Gain profiles of the PA and the NRA. (d) Gain curves of the PA and the NRA represented in a modified Smith chart. The dotted circle refers to a constant gain of 20 dB.

The *ABCD* matrix of a series resonator and that of a parallel resonator are, respectively,

$$T_{\text{ser}} = \begin{bmatrix} 1 & js(\omega)Z_c \\ 0 & 1 \end{bmatrix}, \quad T_{\text{par}} = \begin{bmatrix} 1 & 0 \\ js(\omega)Y_c & 1 \end{bmatrix}, \tag{23}$$

where

$$s(\omega) = \left(\frac{\omega}{\omega_0} - \frac{\omega_0}{\omega}\right) \tag{24}$$

and $Z_c = 1/Y_c = \sqrt{L/C}$ is the characteristic impedance of the resonators.

The total *ABCD* matrix of a PA takes the form

$$T_{\text{PA}} = T_{\text{L}} \times T_{\text{inv}} \times T_{\text{R}}. \tag{25}$$

where T_{inv} is the *ABCD* matrix of the generalized inverter matrix as shown in Fig. 1, and $T_{\text{L}} = T_N T_{N-1} \cdots T_2 T_1$ and $T_{\text{R}} = T_1 T_2 \cdots T_{N-1} T_N$ represent the total *ABCD* matrices of the resonators on the left and right sides of the inverter, where T_i $(i = 1, 2, \ldots, N-1, N)$ is the *ABCD* matrix of the *i*th resonator. The series resonators and parallel resonators appear alternately, and the matrix T_i of each resonator appears twice here. Denoting

$$T_{\text{PA}} = \begin{bmatrix} A_t & jB_t \\ jC_t & D_t \end{bmatrix}, \quad T_{\text{inv}} = \begin{bmatrix} 0 & -j\eta_0 \\ j/\eta_0 & 0 \end{bmatrix} \tag{26}$$

and

$$T_{\text{L}} = \begin{bmatrix} A_{\text{L}} & jB_{\text{L}} \\ jC_{\text{L}} & D_{\text{L}} \end{bmatrix}, \quad T_{\text{R}} = \begin{bmatrix} A_{\text{R}} & jB_{\text{R}} \\ jC_{\text{R}} & D_{\text{R}} \end{bmatrix}, \tag{27}$$

we have $A_{\text{L}} = D_{\text{R}}$, $B_{\text{L}} = B_{\text{R}}$, $C_{\text{L}} = C_{\text{R}}$, $D_{\text{L}} = A_{\text{R}}$, $A_t = D_t$, and $A_t D_t + B_t C_t = -1$. In the series representation,

$\eta_0 = \sqrt{\eta}$. The total power gain (see Appendix E) is given by

$$G_{\mathrm{P}} = (|S_{11}| + |S_{21}|)^2 = 1 + \frac{4Z_{\mathrm{s}}\eta_0}{A_{\mathrm{L}}^2\eta_0^2 + B_{\mathrm{L}}^2 + C_{\mathrm{L}}^2 Z_{\mathrm{s}}^2\eta_0^2 + D_{\mathrm{L}}^2 Z_{\mathrm{s}}^2 - 2Z_{\mathrm{s}}\eta_0}. \quad (28)$$

For an NRA whose load resistance is $-\eta_0$, its input impedance is dependent only on T_{L}:

$$Z_{\mathrm{in,NRA}} = \frac{-A_{\mathrm{L}}\eta_0 + jB_{\mathrm{L}}}{-jC_{\mathrm{L}}\eta_0 + D_{\mathrm{L}}}. \quad (29)$$

The influence of each resonator appears only once. The gain of the NRA is $G_{\mathrm{NRA}} = |(Z_{\mathrm{in,NRA}} - Z_0)/(Z_{\mathrm{in,NRA}} + Z_0)|^2$, and by substituting Eq. (29) into this expression, one can find that the expression for G_{NRA} has the same form as Eq. (28). Consequently, we have

$$G_{\mathrm{NRA}} = G_{\mathrm{P}}. \quad (30)$$

When G_{PA} is high enough,

$$G_{\mathrm{NRA}} \simeq 4G_{\mathrm{PA}}. \quad (31)$$

In the parallel representation, $\eta_0 = -1/\sqrt{\eta^{\alpha}}$, and this leads to the same results. This approach establishes a connection between the impedance matching for a PA and that for an NRA, which is able to circumvent the necessity to consider the impacts of components on both the signal matching network and the idler matching network. As demonstrated in Eq. (31), the gain of a resonator-matched PA with conversion coefficient η_0^2 has a gain approximately a quarter of that of an NRA with a load of $-|\eta_0|$. With this feature and the graphical representation of an NRA in Sec. III, certain impedance-matching methods from conventional microwave circuits find applicability in matching a PA. A $\lambda/4$ transmission line and a $\lambda/2$ transmission line are equivalent to resonators near their characteristic frequency, which makes them suitable for the method [26,31].

Figure 6 presents an example to illustrate the connection between a PA, Fig. 6(a), and the corresponding NRA, Fig. 6(b). In the circuit, Z_{s} is 30 Ω and Z_2 is 10 Ω, which are relatively arbitrary here. $Z_1 = 64$ Ω is chosen to achieve a broad and flat gain profile. The central frequency is 5 GHz. The conversion coefficient η_0^2 is 33.13^2 Ω^2, resulting in a 20-dB gain for the PA at the central frequency, and the load of the NRA is -33.13 Ω. As depicted in Fig. 6(c), the gain profiles of the two amplifiers have the same shape, with G_{NRA} being approximately 6 dB higher than G_{PA}. The cyan line in Fig. 6(c) represents the effective $G'_{\mathrm{NRA}} = G_{\mathrm{NRA}}/4$ of the NRA. It is consistent with the actual gain of the PA, except in the region of small gain, which arises from the approximation in Eq. (31), and is deemed insignificant here. In Fig. 6(d), both G_{PA} and G'_{NRA} are plotted in the modified Smith chart, and coincide well. This approach effectively demonstrates the characteristics of the amplifier, and makes the impedance matching convenient.

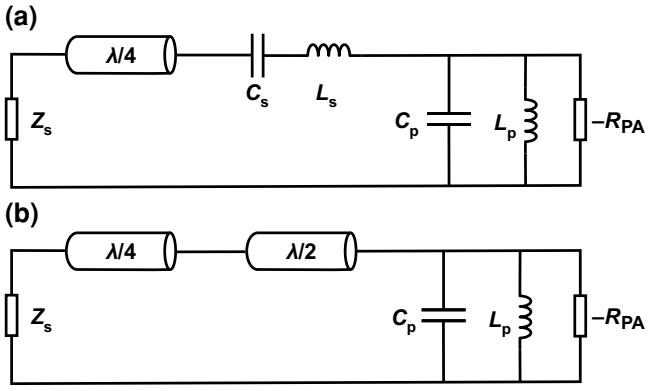

FIG. 7. Two-mode impedance matching of a JPA (a) Circuit diagram of the impedance-matched JPA. The parametrically modulated component is represented by its equivalent negative resistance. The two modes are implemented with lumped resonators. (b) Final circuit diagram of the two-mode impedance-matched JPA. The $\lambda/2$ transmission line serves as a resonator around its characteristic frequency.

V. CASE STUDY

A. Two-mode impedance matching

In the following, we provide several examples demonstrating the use of the modified Smith chart for impedance matching. The first example is a JPA that has the same structure as the design presented by Roy *et al.* [26], which is shown in Fig. 7. It has a large bandwidth, while keeping fabrication easy. In Ref. [26], the design parameters are derived from a physical approach requiring complex calculation. From the perspective of network synthesis, Naaman and Aumentado [31] pointed out that this design is equivalent to synthesizing a two-pole network with Butterworth characteristics.

Here we show how to quickly obtain the corresponding design parameters through the graphical method. In the JPA, the parametrically modulated component is a pumped SQUID whose shunted Josephson inductance L_{p} is resonated out by a capacitor C_{p}. The central frequency of the amplifier is 6 GHz, the shunted capacitor has capacitance of 3.4 pF, and thus the characteristic impedance of the resonator Z_{p} is 7.8 Ω. The amplifier's negative resistance is determined by the target gain. Several methods are used to obtain its value. One way relies on the network-synthesis method. When parameters such as response type (such as a Butterworth response or a Chebyshev response), fractional bandwidth, target gain, and ripple are selected, the

negative resistance can be calculated from the corresponding network coefficients and the characteristic impedance Z_p of the first resonator [31,34]. This method is used in this example, yielding a negative resistance of $-31.8\ \Omega$. Another method is to directly derive the negative resistance from the target gain and the reference impedance of the port, which is discussed in the next subsection. The reference impedance need not be confined to 50 Ω, since it can be transformed by a suitable inverter to a more-amenable value for matching. Estimating the negative resistance directly through the parametric modulation strength is also a viable way. Because parametrically modulated components are generally tunable by bias signals and pumping strength, the negative resistances are also tunable during operation.

In this design, two-mode impedance matching is implemented for the PA. To attain the target gain, a $\lambda/4$ transmission line is introduced between the series resonator and the reference port, as depicted in Fig. 7(a). Because a $\lambda/2$ transmission line has behavior similar to that of the series resonator near the characteristic frequency, the series resonator is replaced by it, as shown in Fig. 7(b), resulting in a schematic that is easier to construct, and this is the circuit diagram that was used in Ref. [26].

With the structure of the matching network established, the next step is to determine the parameters of the components. Figure 8 shows the matching process. Gain curve P1 is for the amplifier before being matched by the two transmission lines. To achieve broadband matching, the gain curve needs to converge to fit a circle as closely as possible. This is accomplished by addition of the $\lambda/2$ transmission line and tuning of its characteristic impedance $Z_{\lambda/2}$. At this step, $Z_{\lambda/2}$ does not have to be precise, and it is chosen to be 50 Ω, initiating the fit of the curve to a circle. The gain curve is shown as curve P2 in the Fig. 8. Next, by addition of the $\lambda/4$ transmission line and tuning of $Z_{\lambda/4}$, the negative impedance at the central frequency is transformed to $-45.5\ \Omega$, with which the central gain is 20 dB. $Z_{\lambda/4}$ is 37.9 Ω here. Meanwhile, the gain curve further converges, as shown by gain curve P3 in Fig. 8. Finally, $Z_{\lambda/2}$ is fine-tuned to be 53.5 Ω so that the gain curve better fits the constant-gain circle in the modified Smith chart, as gain curve P4 shows. The bandwidth becomes wide, and the gain profile becomes flat, as illustrated in Fig. 9. The gain profile G_{PA} is derived from a harmonic-balance (HB) simulation with a SQUID model [31,42]. The critical current of the SQUID I_{SQUID} is 2.8 μA. It is biased at $\Phi_{dc} = 0.3075\Phi_0$, and the pump amplitude $\Phi_{ac} = 0.1108\Phi_0$. The gain profile G'_{NRA} is derived from a simple S-parameter simulation with a negative-resistance model, and it fits well to G_{PA}. $Z_{\lambda/2}$ and $Z_{\lambda/4}$ are, respectively, 58 and 40 Ω in Ref. [26], and 54.55 and 37.93 Ω in Ref. [32], which agree with the values obtained by our approach. The matching process is quickly performed with a Smith chart tool, avoiding intricate calculations.

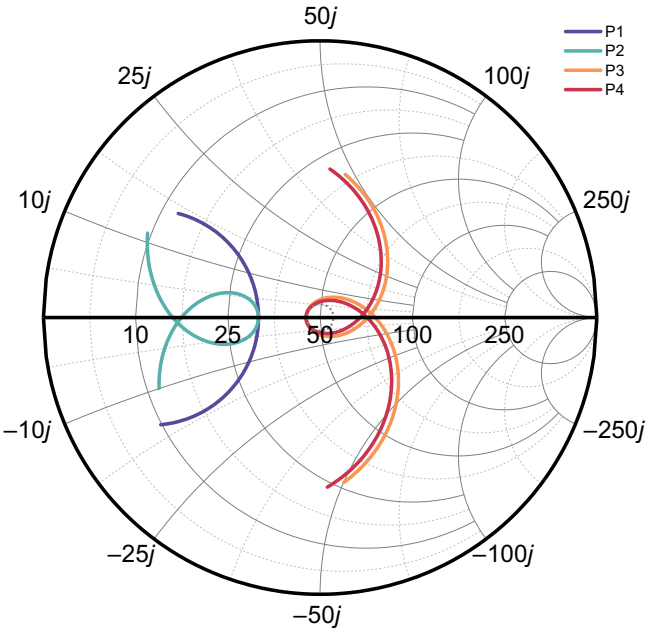

FIG. 8. Matching process for the two-mode JPA. The dotted circle refers to a constant gain of 26 dB. P1, the gain curve before matching by the two transmission lines; P2, the gain curve after the addition of a $\lambda/2$ transmission line with $Z_{\lambda/2} = 50\ \Omega$; P3, the gain curve after the addition of a $\lambda/4$ transmission line with $Z_{\lambda/4} = 37.9\ \Omega$; P4, the final gain curve with $Z_{\lambda/2}$ being fine-tuned to be 53.5 Ω to better fit the constant-gain circle, resulting in a broadband flat gain profile.

By this graphical method, a number of matching structures that are generally difficult to achieve via an analytical approach can be realized. Impedance matching using this method is simple and flexible, and all that left is to let the imagination fly. Figure 10 shows two examples. In Fig. 10(a), the positions of the $\lambda/4$ and $\lambda/2$ transmission lines in Fig. 7(b) are reversed, with $Z_{\lambda/4} = 37.9\ \Omega$ and

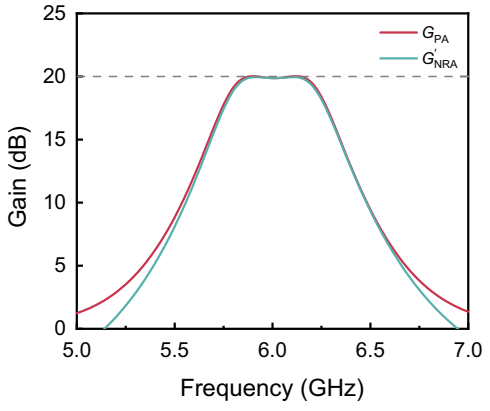

FIG. 9. Gain profiles of the two-mode impedance-matched JPA. The red curve (G_{PA}) is derived from an HB simulation with a SQUID model. The cyan curve (G'_{NRA}) is derived from an S-parameter simulation with a negative-resistance model.

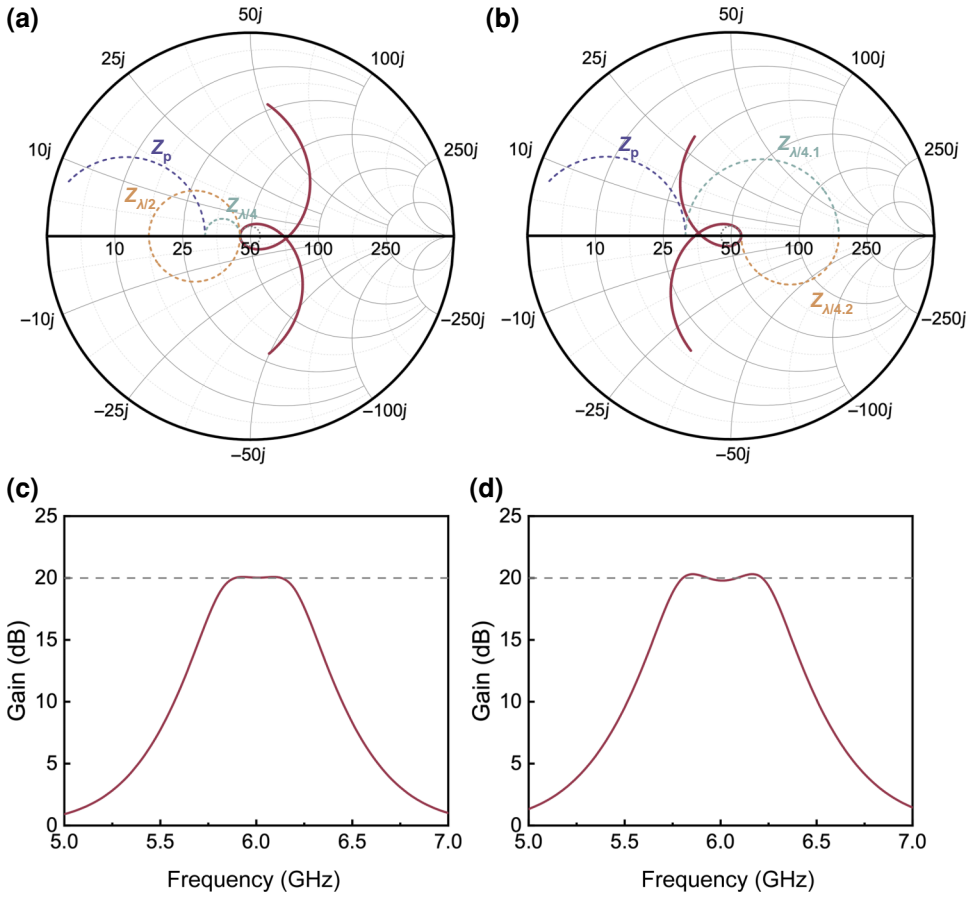

FIG. 10. Graphical impedance matching of a JPA. (a) Matching process for the JPA with a $\lambda/4$ transmission line followed by a $\lambda/2$ transmission line, whose sequence is in contrast to that in Fig. 7(b). The dotted circle refers to a constant gain of 26 dB. (b) Matching process for the JPA with two $\lambda/4$ transmission lines. (c) Gain profile from an HB simulation of the JPA matched with a $\lambda/4$ transmission line and a $\lambda/2$ transmission line. (d) Gain profile from an HB simulation of the JPA matched with two $\lambda/4$ transmission lines.

$Z_{\lambda/2} = 27.5\ \Omega$. The impedance is transformed to $-45.5\ \Omega$ at first, and then $Z_{\lambda/2}$ is tuned to fit the gain curve to the constant-gain circle. The resulting broadband gain profile from an HB simulation is shown in Fig. 10(c), where $\Phi_{dc} = 0.302\Phi_0$ and the pump amplitude Φ_{ac} is $0.112\Phi_0$. When both transmission lines are $\lambda/4$ transmission lines, they are also able to match the amplifier, with $Z_{\lambda/4,1} = 72\ \Omega$ and $Z_{\lambda/4,2} = 95\ \Omega$. The matching process is shown in Fig. 10(b), and the resulting gain profile from an HB simulation is depicted in Fig. 10(d), where $\Phi_{dc} = 0.301\Phi_0$ and $\Phi_{ac} = 0.112\Phi_0$.

B. Four-mode impedance matching

Figure 11(a) shows a JPA matched by a four-mode network, where the reference impedance Z_s is 50 Ω. To achieve a gain of 20 dB, the negative resistance can be directly calculated with Eq. (18), and is $-55.28\ \Omega$ in this circuit. The central frequency is designated as 6 GHz. Resonators are then added to the circuit one by one to increase the bandwidth of the amplifier. The gain curves after the inclusion of each resonator are shown in Fig. 11(b). A useful technique when matching is done with multiple resonators is to introduce a folded structure in the gain curve, which is evident on the addition of the second and third resonators. Finally, a fourth resonator is added to make the curve better fit the constant gain circle. In this circuit, $L_p = 201$ pH, $C_p = 3.5$ pF, $L_2 = 14.19$ pH, $C_2 = 49.59$ fF, $L_3 = 145$ pH, $C_3 = 4.853$ pF, $L_4 = 5.174$ nH, and $C_4 = 136$ fF. Figure 11(c) presents the gain curve obtained with the HB method, where the paramerically modulated inductor is a flux-pumped SQUID and the critical current of the SQUID is 2.8 μA as above. The dc flux bias is $0.2855\Phi_0$ and the pumping strength is $0.0704\Phi_0$. The roll-off of the gain profile is greater than that of the JPA with a two-mode matching network.

This graphical approach involving multiple modes can be combined with the network-synthesis method, increasing understanding of the matching process. If only series and parallel resonators are used for matching, the

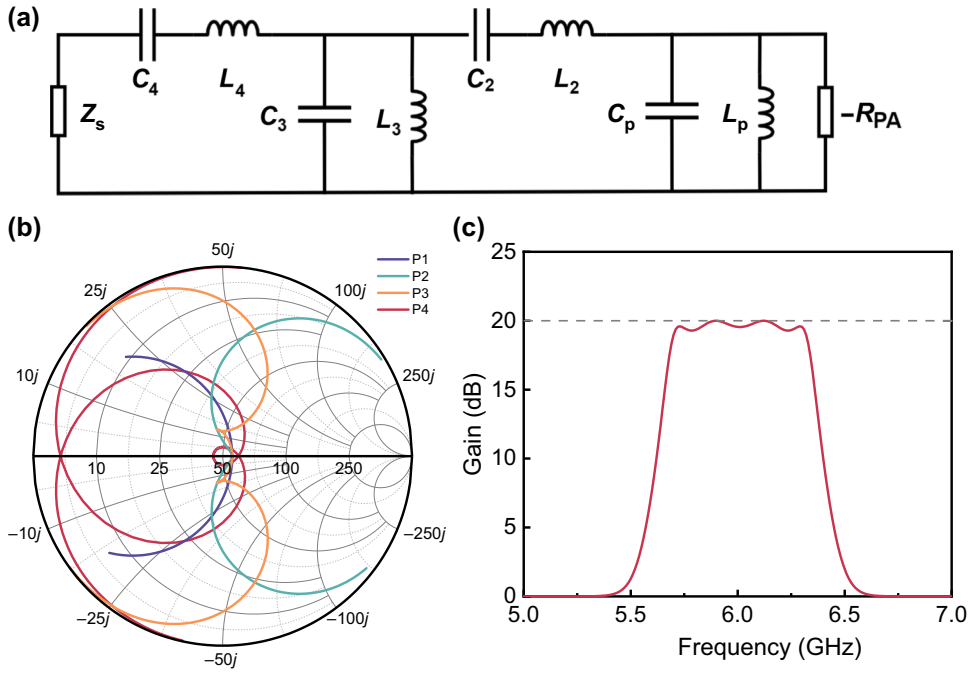

FIG. 11. Four-mode impedance matching of a JPA. (a) Circuit diagram of the four-mode impedance-matched JPA. (b) Matching process for the JPA. P1, P2, P3, and P4 refer to the gain curves after addition of the resonators (from one to four). (c) Gain profile of the four-mode impedance-matched JPA derived from an HB simulation.

parameters of the components might be hard to prepare. The introduction of suitable inverters for additional transformations proves beneficial in addressing this challenge. It is important to note that the component parameters derived from the graphical method are not guaranteed to be optimal. The advantage of the approach is that it is intuitive, fast, and capable of providing many matching networks that might be difficult to obtain through analytical approaches. These networks may offer advantages in physical implementation, such as ease of preparation and area saving.

VI. GRAPHICAL REPRESENTATION FOR THE OPERATING STATE

In practical applications, it is important to locate an appropriate operating state that yields sufficient gain and bandwidth. The operating states are generally set by pump strengths and bias signals. By plotting the variations of the gain with different pump strengths and bias signals on the modified Smith chart, one can express their influences on the gain more clearly, which is helpful to find the optimal operating state and understand the inherent properties of the device.

The effect of pump strength on the behavior of the amplifier is expressed by Eqs. (12) and (13). Variations in pump strength induce changes in the conversion coefficient, consequently leading to different effective negative resistances of the parametrically modulated component. The gain curves of the two-mode impedance-matched JPA from Sec. V under different pump strengths are illustrated in Fig. 12(a). With fixed bias $\Phi_{dc} = 0.3075\Phi_0$, as the pump strength Φ_{ac} increases from $0.09\Phi_0$ to $0.13\Phi_0$, the gain profile becomes narrower and higher, changing from from a broadband flat shape to a single-peak shape. On further increase of the pump strength to $0.15\Phi_0$, the gain decreases, while keeping a single-peak shape. The cause of the phenomenon is apparent from the modified Smith chart, as depicted in Fig. 12(b). The increase in pump strength corresponds to the increase of R_{PA}, and thus the gain curve moves rightward along the x axis. When the central-frequency point resides to the left of the chart center, the gain increases, and since the curve can fit a certain constant-gain circle, a fraction of the gain profiles in Fig. 12(a) remain flat. As the central-frequency point passes the chart center, the gain decreases. It no longer fits any of the constant-gain circles, and therefore the gain profile has a single-peak profile in this region.

The influence of the bias signal is rather complicated, as it affects the constant term L_0 in Eq. (1). For a parametrically modulated inductor whose modulated amplitude δL depends on L_0, such as a flux-pumped SQUID in this instance, the bias signal not only changes the characteristic impedance and resonant frequency of the first resonator but also change the conversion coefficient. As the flux bias Φ_{dc} increases, the gain curves plotted in the modified Smith chart in Fig. 12(d) not only move along the x axis but also rotate by a certain angle. The central-frequency point

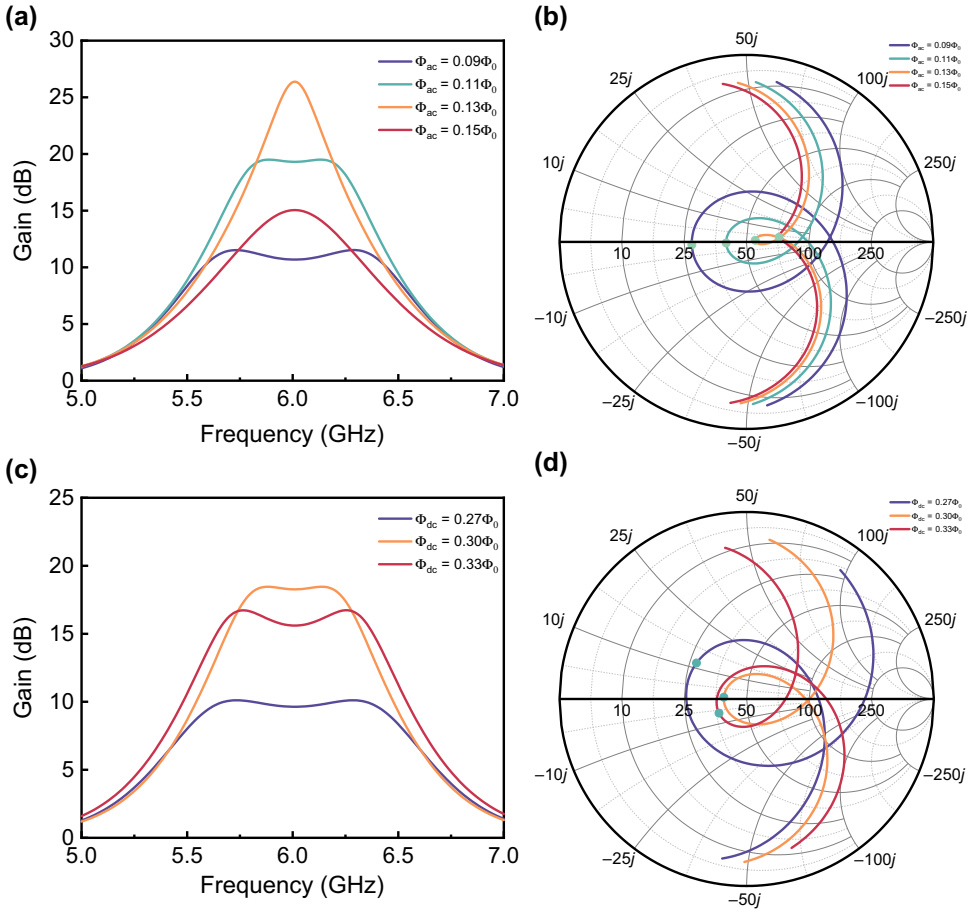

FIG. 12. Parametric amplifiers in different operating states. (a) Gain profiles of the JPA with different pump strengths. (b) Gain curves of the JPA with different pump strengths. The cyan circles refer to the central frequencies. (c) Gain profiles of the JPA with different bias fluxes. (d) Gain curves of the JPA with different bias fluxes. The cyan circles refer to the central frequencies.

no longer falls on the x axis, exhibiting a more-complex behavior. This movement of the central-frequency point is challenging to discern from the gain profiles in Fig. 12(c). The curves in the modified Smith chart provide more-comprehensive insight into the impact of the bias from the perspective of input impedance.

VII. CONCLUSION

This work proposes a graphical method for impedance matching superconducting parametric amplifiers with quantum-limited noise performance. A parametrically modulated component, the core of a PA, is represented as a generalized inverter sandwiched by two associated components. The inverter interconnects the matching networks at signal and idler frequencies. This connection prevents a PA from being regarded as an ideal NRA during the matching process. Every element added to the physical matching network impacts both the signal-frequency network and the idler-frequency network, making the matching of the PA complicated. Nonetheless, as pointed out in this paper, if the matching network comprises resonators or resonator-equivalent components, the PA can be regarded as an NRA, whose negative resistance is determined by the conversion coefficient. This work presents a simple but effective method to represent negative-resistance circuits on a Smith chart for NRAs. The method facilitates matching a PA with resonators and their equivalents conveniently and quickly, circumventing the need for intricate calculations. Matching networks that are difficult to obtain by analytical methods are also attainable with this method. It enables one to rapidly apply the impedance-matching methods from microwave engineering to PAs. On the modified Smith chart, how pump strengths and bias signals affect the gain curve by changing the negative resistance and the resonant frequency of the circuit is elucidated clearly, which helps to capture the physical characteristics of the device and identify the optimal operating point. This approach bridges the gap between conventional microwave matching methods and the matching of PAs,

helping design PAs with better performance and simplify the matching process. Further work is required to incorporate nonresonator components into the matching of PAs and optimize the quantum noise performance of the device with this method.

ACKNOWLEDGMENTS

This work is supported by the Nation Key Research and Development Program of China (Grant No. 2022YFC22 05101).

APPENDIX A: MODULATED JOSEPHSON JUNCTIONS AND SQUIDS

There are various devices based on Josephson junctions that are able to act as parametrically modulated inductors. Depending on the settings, they operate in three-wave-mixing mode or four-wave-mixing mode, which satisfies $\omega_p = \omega_s + \omega_i$ or $2\omega_p = \omega_s + \omega_i$, respectively. The pump tone can be current or magnetic flux. Here, two basic models are introduced, which are a current-pumped Josephson junction and a flux-pumped SQUID.

1. Current-pumped Josephson junction

From the two basic Josephson equations, the effective inductance of a single Josephson junction is given by

$$L_J(I) = \frac{\Phi_0}{2\pi I_c \cos(\phi)} = \frac{\Phi_0}{2\pi I_c}\frac{1}{\sqrt{1 - I^2/I_c^2}}, \tag{A1}$$

where $\Phi_0 = h/2e$ is the flux quantum, I_c is the critical current of the Josephson junction, and ϕ is the gauge-invariant phase across the junction.

When the pump tone is applied by an unbiased current $I_p(t) = |I_p|\cos(\omega_p t + \phi_p)$ with $|I_p| \ll I_c$ and the effective inductance is expanded to the first order of I^2, we have

$$\begin{aligned} L_J(I) &\simeq \frac{\Phi_0}{2\pi I_c}\left(1 + \frac{I^2}{2I_c^2}\right) \\ &= L_{J0}\left[1 + \frac{|I_p|^2}{2I_c^2}\cos^2(\omega_p t + \phi_p)\right] \\ &= L_0 + 2|\delta L|\cos(2\omega_p t + 2\phi_p), \end{aligned} \tag{A2}$$

where

$$L_0 = L_{J0}\left(1 + \frac{|I_p|^2}{4I_c^2}\right) \tag{A3}$$

is the constant term in the modulated inductance, which is dependent on the pump current. $L_{J0} = \Phi_0/2\pi I_c$ is the Josephson inductance of a single junction. The modulated amplitude is given by

$$|\delta L| = \frac{L_{J0}}{8}\frac{|I_p|^2}{I_c^2}. \tag{A4}$$

Note that the modulation frequency in Eq. (A2) is $2\omega_p$, and thus this is the four-wave-mixing mode. In a physical view, two pump photons are annihilated, producing a signal photon and an idler photon. The four-wave mixing is a result of the quadratic nonlinearity in Eq. (A2). If the pump signal is biased by a direct current, the quadratic nonlinearity is broken down, and the four-wave mixing does not play a dominant role.

For a pump current $I_p(t) = I_{dc} + |I_p|\cos(\omega_p t + \phi_p)$, the effective inductance of the junction is given by

$$\begin{aligned} L_J(I) &= L_{J0}\frac{1}{\sqrt{1 - \frac{[I_{dc} + |I_p|\cos(\omega_p t + \phi_p)]^2}{I_c^2}}} \\ &\simeq L_{J0}\frac{1}{\sqrt{1 - \frac{I_{dc}^2 + 2I_{dc}|I_p|\cos(\omega_p t + \phi_p)}{I_c^2}}} \\ &= \frac{L_{J0}}{\sqrt{1 - I_{dc}^2/I_c^2}}\frac{1}{\sqrt{1 - \frac{2I_d|I_p|}{I_c^2(1 - I_{dc}^2/I_c^2)}\cos(\omega_p t + \phi_p)}} \\ &\simeq L_0 + 2|\delta L|\cos(\omega_p t + \phi_p), \end{aligned} \tag{A5}$$

where

$$L_0 = \frac{L_{J0}}{\sqrt{1 - I_{dc}^2/I_c^2}} \tag{A6}$$

is the constant inductance, which is dependent on the dc bias instead of the amplitude of the alternating current. The modulated amplitude is given by

$$|\delta L| = L_{J0}\frac{I_c I_{dc}|I_p|}{2(I_c^2 - I_{dc}^2)^{3/2}}. \tag{A7}$$

In Eq. (A5), the pump frequency is ω_p, and thus this is the three-wave-mixing mode, since the dominant first-order expansion term in the current is linear. The annihilation of a pump photon leads to the production of a signal photon and an idler photon. The parametrically modulated inductance of a single Josephson junction can also be found in Ref. [31].

2. Flux-pumped SQUID

A dc SQUID is composed of two parallel Josephson junctions forming a loop. The effective inductance of the

dc SQUID is controlled by the magnetic flux threading the loop:

$$L_{\mathrm{SQUID}} = \frac{L_{\mathrm{J0}}(I)}{2|\cos(\pi\Phi_{\mathrm{ext}}/\Phi_0)|}, \tag{A8}$$

where $L_{\mathrm{J0}}(I)$ is the Josephson inductance of a junction, and the two junctions are assumed to be identical.

For an unbiased pump flux $\Phi_{\mathrm{ext}} = \Phi_{\mathrm{p}}\cos(\omega_{\mathrm{p}}t + \phi_{\mathrm{p}})$ with Φ_{p} near zero, the inductance of the SQUID is given by

$$\begin{aligned} L_{\mathrm{SQUID}} &= \frac{L_{\mathrm{J0}}(I)}{2\cos\left[\frac{\pi\Phi_{\mathrm{p}}}{\Phi_0}\cos(\omega_{\mathrm{p}}t+\phi_{\mathrm{p}})\right]} \\ &\simeq \frac{L_{\mathrm{J0}}(I)}{2\left[1-\frac{\pi^2\Phi_{\mathrm{p}}^2}{2\Phi_0^2}\cos^2(\omega_{\mathrm{p}}t+\phi_{\mathrm{p}})\right]} \\ &\simeq L_0 + 2|\delta L|\cos(2\omega_{\mathrm{p}}t + 2\phi_p), \end{aligned} \tag{A9}$$

where the constant inductance is given by

$$L_0 = \frac{L_{\mathrm{J0}}(I)}{2(1-\pi^2\Phi_{\mathrm{p}}^2/4\Phi_0^2)} \simeq \frac{L_{\mathrm{J0}}(I)}{2} \tag{A10}$$

and the modulated amplitude is given by

$$|\delta L| = L_{\mathrm{J0}}(I)\frac{\pi^2\Phi_{\mathrm{p}}^2}{16\Phi_0^2}. \tag{A11}$$

The pumping frequency in Eq. (A9) is $2\omega_{\mathrm{p}}$, and it works in the four-wave-mixing mode. The modulated SQUID can also work in the three-wave-mixing mode, as long as a dc bias flux is applied to the pump tone, $\Phi_{\mathrm{ext}} = \Phi_{\mathrm{dc}} + \Phi_{\mathrm{p}}\cos(\omega_{\mathrm{p}}t + \phi_{\mathrm{p}})$, where Φ_{dc} is near $(n+1)\Phi_0$. The leading first-order expansion term in the flux is linear. In this case, the modulated inductance is given by

$$\begin{aligned} L_{\mathrm{SQUID}} &= \frac{L_{\mathrm{J0}}(I)}{2\cos\left(\pi\frac{\Phi_{\mathrm{dc}}}{\Phi_0} + \pi\frac{\Phi_{\mathrm{p}}}{\Phi_0}\cos(\omega_{\mathrm{p}}t+\phi_{\mathrm{p}})\right)} \\ &\simeq \frac{L_{\mathrm{J0}}(I)}{2\cos(\pi\frac{\Phi_{\mathrm{dc}}}{\Phi_0}) - 2\pi\frac{\Phi_{\mathrm{p}}}{\Phi_0}\sin\left(\pi\frac{\Phi_{\mathrm{dc}}}{\Phi_0}\right)\cos(\omega_{\mathrm{p}}t+\phi_{\mathrm{p}})} \\ &= \frac{L_{\mathrm{J0}}(I)}{2\cos\left(\pi\frac{\Phi_{\mathrm{dc}}}{\Phi_0}\right)} \\ &\quad\times\frac{1}{1-\pi\frac{\Phi_{\mathrm{p}}}{\Phi_0}\tan\left(\pi\frac{\Phi_{\mathrm{dc}}}{\Phi_0}\right)\cos(\omega_{\mathrm{p}}t+\phi_{\mathrm{p}})} \\ &\simeq L_0 + 2|\delta L|\cos(\omega_{\mathrm{p}}t+\phi_p), \end{aligned} \tag{A12}$$

where

$$L_0 = \frac{L_{\mathrm{J0}}(I)}{2\cos(\pi\Phi_{\mathrm{dc}}/\Phi_0)} \tag{A13}$$

and

$$|\delta L| = L_0\frac{\pi\Phi_{\mathrm{p}}}{2\Phi_0}\tan\left(\frac{\pi\Phi_{\mathrm{dc}}}{\Phi_0}\right). \tag{A14}$$

Similar treatment of the pumped SQUID is presented in Ref. [41]. Some nonlinear terms are handled differently. However, for small pump amplitudes, this does not lead to a significant difference in the result.

APPENDIX B: INPUT-OUTPUT THEORY FOR A PARAMETRIC AMPLIFIER

In this appendix, we show how the equation of motion for a pumped PA and the susceptibility matrix are obtained from the input-output theory. From Sec. II, we see that the Hamiltonian of a single pumped LC resonator is as follows:

$$\hat{H}_{\mathrm{sys}} = \hbar\omega_0\left[\hat{a}^\dagger\hat{a} + (\alpha e^{-i\omega_{\mathrm{p}}t} + \alpha^\star e^{i\omega_{\mathrm{p}}t})(\hat{a}+\hat{a}^\dagger)^2\right]. \tag{B1}$$

When it is connected to a port, it is exposed not only to the external drive but also to the vacuum noise outside, which allows energy in the resonator to leak out to the surrounding bath. The total Hamiltonian is as follows:

$$\hat{H} = \hat{H}_{\mathrm{sys}} + \hat{H}_{\mathrm{bath}} + \hat{H}_{\mathrm{int}}. \tag{B2}$$

$\hat{H}_{\mathrm{bath}}$ is the bath Hamiltonian:

$$\hat{H}_{\mathrm{bath}} = \sum_k \hbar\omega_k\hat{b}_k^\dagger\hat{b}_k, \tag{B3}$$

where k denotes the quantum numbers of the independent harmonic oscillator bath modes, and $[\hat{b}_k, \hat{b}_{k'}^\dagger] = \delta_{k,k'}$. The interaction Hamiltonian is as follows:

$$\hat{H}_{\mathrm{int}} = -i\hbar\sum_k\left[g_k\hat{a}^\dagger\hat{b}_k - g_k^\star\hat{b}_k^\dagger\hat{a}\right]. \tag{B4}$$

The rotating-wave approximation is applied here, and g_k is the coupling strength between the bath modes and the resonator mode.

The Heisenberg equations of motion for $\hat{a}$ and $\hat{b}_k$ are as follows:

$$\begin{aligned} \frac{\mathrm{d}\hat{a}}{\mathrm{d}t} &= \frac{i}{\hbar}[\hat{H},\hat{a}] \\ &= -i\omega_0\hat{a} - 2i\omega_0(\alpha e^{-i\omega_{\mathrm{p}}t} + \alpha^\star e^{i\omega_{\mathrm{p}}t})(\hat{a}+\hat{a}^\dagger) - \sum_k g_k\hat{b}_k \end{aligned} \tag{B5}$$

and

$$\frac{\mathrm{d}\hat{b}_k}{\mathrm{d}t} = \frac{i}{\hbar}[\hat{H},\hat{b}_k] = -i\omega_k\hat{b}_k + g_k^\star\hat{a}. \tag{B6}$$

The equation for the bath operator $\hat{b}_k$ can be formally integrated to yield

$$\hat{b}_k(t) = \hat{b}_k(0)e^{-i\omega_k t} + \int_0^t \mathrm{d}t' g_k^\star \hat{a}(t')e^{-i\omega_k(t-t')}. \tag{B7}$$

The first term represents the free evolution of the bath, while the second term arises from the interaction with the resonator. Substituting Eq. (B7) into the last term of Eq. (B5) yields

$$\sum_k g_k \hat{b}_k = \sum_k g_k e^{-i\omega_k t}\hat{b}_k(0) + \sum_k \int_0^t \mathrm{d}t' |g_k|^2 e^{-i(\omega_k-\omega_0)(t-t')}\left[e^{i\omega_0(t'-t)}\hat{a}(t')\right]. \tag{B8}$$

Using the Fermi golden rule and making the Markov approximation [2,54], we obtain

$$\sum_k |g_k|^2 e^{-i(\omega_k-\omega_0)(t-t')} = \kappa\delta(t-t'), \tag{B9}$$

where κ is the dissipation rate. When the coupling strength is further treated as a constant $g \equiv \sqrt{|g_k|^2}$ and the density of states is defined as

$$\rho \equiv \sum_k \delta(\omega_0 - \omega_k), \tag{B10}$$

the dissipation rate is as follows:

$$\kappa = 2\pi g^2 \rho. \tag{B11}$$

With

$$\int_0^t \mathrm{d}t' \delta(t-t') = \frac{1}{2}, \tag{B12}$$

the second term in Eq. (B8) is

$$\sum_k \int_0^t \mathrm{d}t' |g_k|^2 e^{-i(\omega_k-\omega_0)(t-t')}\left[e^{i\omega_0(t'-t)}\hat{a}(t')\right] = \frac{\kappa}{2}\hat{a}. \tag{B13}$$

The first term in Eq. (B8) can be defined as the so-called input mode

$$\hat{a}_{\mathrm{in}} \equiv \frac{1}{\sqrt{2\pi\rho}}\sum_k e^{-i\omega_k t}\hat{b}_k(0), \tag{B14}$$

and thus the equation of motion for $\hat{a}$ is

$$\frac{\mathrm{d}\hat{a}}{\mathrm{d}t} = \left(-i\omega_0 - \frac{\kappa}{2}\right)\hat{a} - 2i\omega_0(\alpha e^{-i\omega_\mathrm{p} t} + \alpha^\star e^{i\omega_\mathrm{p} t})(\hat{a}+\hat{a}^\dagger) - \sqrt{\kappa}\hat{a}_{\mathrm{in}}. \tag{B15}$$

The susceptibility matrix is derived from the equation of motion in the frequency domain. The Fourier transform of $\hat{a}(t)$ is defined as

$$\mathcal{F}\left[\hat{a}(t)\right] \equiv \hat{a}(\omega) = \frac{1}{\sqrt{2\pi}}\int_{-\infty}^{\infty}\mathrm{d}t\hat{a}(t)e^{i\omega t}, \tag{B16}$$

and its Hermitian conjugate is as follows:

$$\mathcal{F}^\dagger\left[\hat{a}(t)\right] \equiv \hat{a}^\dagger(\omega) = \frac{1}{\sqrt{2\pi}}\int_{-\infty}^{\infty}\mathrm{d}t\hat{a}^\dagger(t)e^{-i\omega t}. \tag{B17}$$

The Fourier transform of $\hat{a}^\dagger(t)$ is therefore given by

$$\mathcal{F}\left[\hat{a}^\dagger(t)\right] = \frac{1}{\sqrt{2\pi}}\int_{-\infty}^{\infty}\mathrm{d}t\hat{a}^\dagger(t)e^{i\omega t} = \hat{a}^\dagger(-\omega). \tag{B18}$$

Multiplying both sides of Eq. (B15) by $\exp(i\omega_\mathrm{p} t/2)$ and then performing the Fourier transform leads to the equation of motion in the frequency domain (within the rotating-wave approximation):

$$(-i\omega_\mathrm{s} + i\omega_0 + \kappa/2)\hat{a}(\omega_\mathrm{s}) + 2i\omega_0\alpha\hat{a}^\dagger(\omega_\mathrm{i}) = \sqrt{\kappa}\hat{a}_{\mathrm{in}}(\omega_\mathrm{s}), \tag{B19}$$

where ω_s and ω_i are as defined in Sec. II. The same calculation performed on the conjugate of Eq. (B15) yields

$$-2i\omega_0\alpha^\star\hat{a}^\dagger(\omega_\mathrm{s}) + (i\omega_\mathrm{i} - i\omega_0 + \kappa/2)\hat{a}(\omega_\mathrm{s}) = \sqrt{\kappa}\hat{a}^\dagger_{\mathrm{in}}(\omega_\mathrm{i}). \tag{B20}$$

Therefore, the susceptibility matrix $\chi(\omega_\mathrm{s})$ that connects the intracavity field and the input field $\vec{a} = \chi(\omega_\mathrm{s})\sqrt{\kappa}\vec{a}_{\mathrm{in}}$ is given by

$$[\chi(\omega_\mathrm{s})]^{-1} = -i\begin{bmatrix}\omega_\mathrm{s} - \omega_0 + i\kappa/2 & -2\omega_0\alpha \\ 2\omega_0\alpha^\star & -\omega_\mathrm{i} + \omega_0 + i\kappa/2\end{bmatrix}. \tag{B21}$$

APPENDIX C: *ABCD* MATRIX

In the microwave field, many networks are composed of a cascade of several two-port networks. It is convenient to describe the individual two-port networks in the cascaded system with a transmission (T or $ABCD$) matrix, since the properties of the entire system can be obtained by directly multiplying the $ABCD$ matrices [44].

It is easy to find the $ABCD$ matrix of a two-port network from its Z matrix, and vice versa. Use of the $ABCD$ matrix allows the decomposition of a network into a series of multiplied simpler networks, offering a more-direct grasp of the network's characteristics. From the Z matrix, the

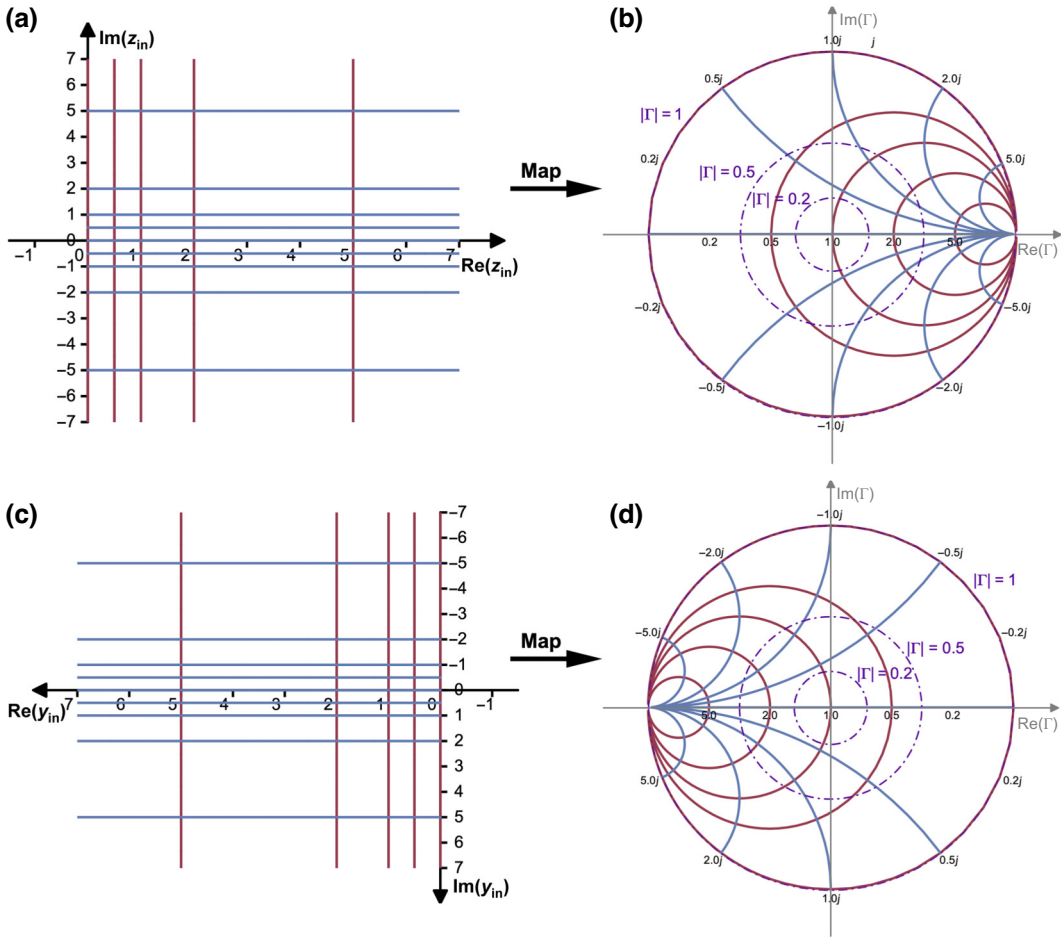

FIG. 13. Principle of the conventional Smith chart. (a),(b) Input-impedance z_{in} plane and the reflection-coefficient Γ plane. The constant-resistance (red) and constant-reactance (blue) lines in the z_{in} plane are mapped to be circles in the Γ plane. The tick values of Γ in (b) are represented by the purple circles. (c),(d) Input-admittance y_{in} plane and reflection-coefficient Γ plane. The constant-conductance (red) and constant-susceptance (blue) lines in the y_{in} plane are mapped to be circles in the Γ plane.

ABCD matrix is as follows:

$$\begin{bmatrix} A & B \\ C & D \end{bmatrix} = \begin{bmatrix} Z_{11}/Z_{21} & |Z|/Z_{21} \\ 1/Z_{21} & Z_{22}/Z_{21} \end{bmatrix} = \begin{bmatrix} 1 & Z_{11} \\ 0 & 1 \end{bmatrix} \begin{bmatrix} 0 & -Z_{12} \\ Z_{21}^{-1} & 0 \end{bmatrix} \begin{bmatrix} 1 & Z_{22} \\ 0 & 1 \end{bmatrix}, \quad \text{(C1)}$$

where $|Z| = Z_{11}Z_{22} - Z_{12}Z_{21}$. The matrix with the upper triangle form in Eq. (C1) corresponds to a two-port network composed of a series component. The off-diagonal matrix represents an inverter network. Figure 1(b) shows this sandwiched structure.

It is also feasible to obtain the *ABCD* matrix from the *Y* matrix:

$$\begin{bmatrix} A & B \\ C & D \end{bmatrix} = \begin{bmatrix} -Y_{22}/Y_{21} & -1/Y_{21} \\ -|Y|/Y_{21} & -Y_{11}/Y_{21} \end{bmatrix} \quad \text{(C2)}$$

$$= \begin{bmatrix} 1 & 0 \\ Y_{11} & 1 \end{bmatrix} \begin{bmatrix} 0 & -Y_{21}^{-1} \\ Y_{12} & 0 \end{bmatrix} \begin{bmatrix} 1 & 0 \\ Y_{22} & 1 \end{bmatrix}, \quad \text{(C3)}$$

where $|Y| = Y_{11}Y_{22} - Y_{12}Y_{21}$. It similarly portrays a sandwiched configuration, with the network on either side no longer being series impedance, but rather parallel admittance, as illustrated by the lower triangle matrices in Eq. (C3). The circuit representation of this structure is shown in Fig. 1(c).

Given the reference impedance Z_s of the port, the *S* parameter of the system can be obtained:

$$\begin{bmatrix} S_{11} & S_{12} \\ S_{21} & S_{22} \end{bmatrix} = \begin{bmatrix} \frac{A+B/Z_s-CZ_s-D}{\Delta} & \frac{2(AD-BC)}{\Delta} \\ \frac{2}{\Delta} & \frac{-A+B/Z_s-CZ_s+D}{\Delta} \end{bmatrix}, \quad \text{(C4)}$$

where $\Delta = A + B/Z_s + CZ_s + D$.

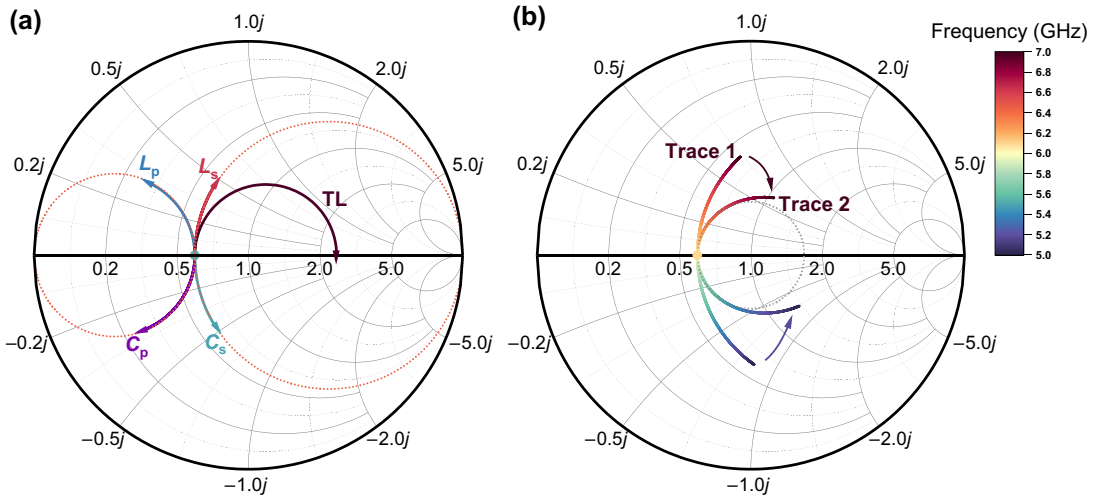

FIG. 14. Impedance matching with the conventional Smith chart. (a) Impact of the basic components on the input impedance, including series inductors (L_s), series capacitors (C_s), parallel inductors (L_p), parallel capacitors (C_p), and transmission lines (TL). (b) Impact of the components at different frequencies. The dotted circle refers to a VSWR circle of 1.667.

APPENDIX D: CONVENTIONAL SMITH CHART

The Smith chart is an effective tool for impedance matching in the microwave field. It simultaneously displays impedance and its corresponding reflection coefficient on a single chart. The Smith chart is based on the equation

$$\Gamma = \frac{z_{\text{in}} - 1}{z_{\text{in}} + 1}, \tag{D1}$$

where $z_{\text{in}} = Z_{\text{in}}/Z_s$ is the normalized input impedance seen from the reference port. It is a conformal transformation [39], which maps the constant-resistance and constant-reactance lines in the z_{in} plane to a series of circles in the Γ plane, as shown in Figs. 13(a) and 13(b). The reactance circles are not entirely within the chart. The tick values in Fig. 13(b) are those of the constant-resistance and constant-reactance circles. The tick values of Γ are not shown, but are represented by a series of circles (the purple circles). The entire non-negative-resistance region of the z_{in} plane is mapped into a unit circle in the Γ plane, and it is the Smith chart. In the same way, the admittance circles can be mapped to the Γ plane, as shown in Figs. 13(c) and 13(d). Use of the Smith Chart facilitates the derivation of reflection coefficients from circuit impedance or admittance, and vice versa.

The effects of adding capacitors and inductors to the circuit are effectively elucidated with use of a Smith chart. As illustrated in Fig. 14(a), when a series inductor L_s or a series capacitor C_s is added to the circuit, the reactance part of z_{in} is changed, causing it to move along the constant-resistance circle clockwise or counterclockwise, respectively. Similarly, after introduction of a parallel inductor L_p or a parallel capacitor C_p, z_{in} moves along the constant-conductance circle. If a transmission line with normalized characteristic impedance z_{TL} and length λ_{TL} is introduced to the circuit, z_{in} rotates by an angle of $4\pi\lambda_{\text{TL}}/\lambda_0$, with z_{TL} as the center, where λ_0 is the wavelength at the corresponding frequency [39,44]. By strategic arrangement of these components, z_{in} is moved along the circles, and it finally reaches the desired impedance and reflection coefficient.

Since the impedance of most components is frequency dependent, their impact on z_{in} also varies with the frequency. Figure 14(b) shows an illustrative example. Trace 1 depicts the frequency response of a series *RLC* resonator with $R = 30\ \Omega$, $L = 3$ nH, and $C = 234.5$ fF. The reference impedance Z_s is 50 Ω. With a parallel *LC* resonator introduced into the circuit, where $L' = 1$ nH and $C' = 0.7036$ pF, the frequency response becomes that of trace 2. The impedance at the central frequency, which is 6 GHz, remains unchanged. However, the impedance at other frequencies undergoes varying degrees of change, leading to alternations in bandwidth, which is clearly depicted with a criterion circle in the Smith chart, such as a VSWR circle or a constant-gain circle.

APPENDIX E: SIGNAL AMPLITUDE GAIN AND INTERMODULATION AMPLITUDE GAIN

For a parametric amplifier, there is a relation between its signal gain S_{11} and its intermodulation gain S_{21}:

$$|S_{11}|^2 - |S_{21}|^2 = 1. \tag{E1}$$

It can be directly validated from Eqs. (6) and (7),and their corresponding generalized forms. Here, we provide a proof using the lumped-circuit approach.

Firstly, when the circuit contains only one resonator, the total *ABCD* matrix in the series representation is as follows:

$$T_{\text{total}} = \begin{bmatrix} 1 & jsZ_c \\ 0 & 1 \end{bmatrix} \begin{bmatrix} 0 & -j\eta_0 \\ j/\eta_0 & 0 \end{bmatrix} \begin{bmatrix} 1 & jsZ_c \\ 0 & 1 \end{bmatrix} = \begin{bmatrix} -sZ_c/\eta_0 & -j\left(s^2 Z_c/\eta_0 + \eta_0\right) \\ j/\eta_0 & -sZ_c/\eta_0 \end{bmatrix} = \begin{bmatrix} A_1 & jB_1 \\ jC_1 & D_1 \end{bmatrix}, \tag{E2}$$

where $A_1, B_1, C_1, D_1 \in \mathbb{R}$ and $s = s(\omega_s) = s(-\omega_i)$. The diagonal elements in this matrix are real, while the nondiagonal elements are imaginary. Given that $\det(T_{\text{total}}) = A_1 D_1 + B_1 D_1 = -1$, we have

$$\begin{aligned} |S_{11}|^2 - |S_{21}|^2 &= \frac{(A_1 - D_1)^2 + (B_1/Z_s - C_1 Z_s)^2 - 4}{(A_1 + D_1)^2 + (B_1/Z_s + C_1 Z_s)^2} \\ &= 1 + \frac{-4(A_1 D_1 + B_1 C_1 + 1)}{(A_1 + D_1)^2 + (B_1/Z_s + C_1 Z_s)^2} \\ &= 1. \end{aligned} \tag{E3}$$

When an extra resonator is incorporated, the new *ABCD* matrix is as follows:

$$T'_{\text{total}} = \begin{bmatrix} 1 & 0 \\ jsY_c & 1 \end{bmatrix} \begin{bmatrix} A_1 & jB_1 \\ jC_1 & D_1 \end{bmatrix} \begin{bmatrix} 1 & 0 \\ jsY_c & 1 \end{bmatrix} = \begin{bmatrix} A_2 & jB_2 \\ jC_2 & D_2 \end{bmatrix}, \tag{E4}$$

where $A_2, B_2, C_2, D_2 \in \mathbb{R}$. The diagonal elements remain real, and the nondiagonal elements continue to be imaginary. Additionally, $\det(T'_{\text{total}}) = A_2 D_2 + B_2 D_2 = -1$. Consequently, Eq. (E3) holds for T'_{total}. As more resonators are introduced, this property of the total *ABCD* matrix persists, thereby confirming the relationship of Eq. (E1). It can also be proved similarly under the parallel representation.

Below, we show the equivalence between G_P and G_{NRA}. The total power gain G_P in Eq. (28) is given by

$$\begin{aligned} G_P &= (|S_{11}| + |S_{21}|)^2 \\ &= \frac{\left[\sqrt{(A_t - D_t)^2 + (B_t/Z_s - C_t Z_s)^2} + 2\right]^2}{(A_t + D_t)^2 + (B_t/Z_s + C_t Z_s)^2} \\ &= 1 + \frac{8 + 4|B_t/Z_s - C_t Z_s|}{(A_t + D_t)^2 + (B_t/Z_s + C_t Z_s)^2} \\ &= 1 + \frac{8 + 4Z_s \frac{(C_L^2 \eta_0^2 + D_L^2)}{\eta_0} + 4\frac{(A_L^2 \eta_0^2 + B_L^2)}{Z_s \eta_0}}{4\frac{\left(A_L C_L \eta_0^2 - B_L D_L\right)^2}{\eta_0^2} + \frac{\left[-\frac{A_L^2 \eta_0^2 + B_L^2}{Z_s} + Z_s(C_L^2 \eta_0^2 + D_L^2)\right]^2}{\eta_0^2}} \\ &= 1 + \frac{4Z_s \eta_0}{A_L^2 \eta_0^2 + B_L^2 + C_L^2 Z_s^2 \eta_0^2 + D_L^2 Z_s^2 - 2Z_s \eta_0}, \end{aligned} \tag{E5}$$

where we have used the transformation from the *ABCD* matrix to the scattering matrix, Eq. (C4). In an NRA, the power gain is as follows:

$$\begin{aligned} G_{NRA} &= \left|\frac{Z_{\text{in, NRA}} - Z_0}{Z_{\text{in,NRA}} + Z_0}\right|^2 \\ &= 1 + \frac{4(A_L D_L + B_L C_L)\eta_0/Z_s}{(-A_L \eta_0/Z_s + D_L)^2 + (B_L/Z_s - C_L \eta_0)^2} \\ &= 1 + \frac{4Z_s \eta_0}{A_L^2 \eta_0^2 + B_L^2 + C_L^2 Z_s^2 \eta_0^2 + D_L^2 Z_s^2 - 2Z_s \eta_0}. \end{aligned} \tag{E6}$$

Therefore, we have

$$G_{NRA} = G_P. \tag{E7}$$

[1] C. M. Caves, Quantum limits on noise in linear amplifiers, Phys. Rev. D **26**, 23 (1982).

[2] A. A. Clerk, M. H. Devoret, S. M. Girvin, F. Marquardt, and R. J. Schoelkopf, Introduction to quantum noise, measurement, and amplification, Rev. Mod. Phys. **82**, 1155 (2010).

[3] P. Krantz, M. Kjaergaard, F. Yan, T. P. Orlando, S. Gustavsson, and W. D. Oliver, A quantum engineer's guide to superconducting qubits, Appl. Phys. Rev. **6**, 021318 (2019).

[4] F. Arute, *et al.*, Quantum supremacy using a programmable superconducting processor, Nature **574**, 505 (2019).

[5] B. Yurke, L. R. Corruccini, P. G. Kaminsky, L. W. Rupp, A. D. Smith, A. H. Silver, R. W. Simon, and E. A. Whittaker, Observation of parametric amplification and deamplification in a Josephson parametric amplifier, Phys. Rev. A **39**, 2519 (1989).

[6] M. A. Castellanos-Beltran and K. W. Lehnert, Widely tunable parametric amplifier based on a superconducting quantum interference device array resonator, Appl. Phys. Lett. **91**, 083509 (2007).

[7] T. Yamamoto, K. Inomata, M. Watanabe, K. Matsuba, T. Miyazaki, W. D. Oliver, Y. Nakamura, and J. S. Tsai, Flux-driven Josephson parametric amplifier, Appl. Phys. Lett. **93**, 042510 (2008).

[8] R. Vijay, D. H. Slichter, and I. Siddiqi, Observation of quantum jumps in a superconducting artificial atom, Phys. Rev. Lett. **106**, 110502 (2011).

[9] B. Abdo, F. Schackert, M. Hatridge, C. Rigetti, and M. Devoret, Josephson amplifier for qubit readout, Appl. Phys. Lett. **99**, 162506 (2011).

[10] B. Abdo, K. Sliwa, S. Shankar, M. Hatridge, L. Frunzio, R. Schoelkopf, and M. Devoret, Josephson directional amplifier for quantum measurement of superconducting circuits, Phys. Rev. Lett. **112**, 167701 (2014).

[11] B. Abdo, O. Jinka, N. T. Bronn, S. Olivadese, and M. Brink, High-fidelity qubit readout using interferometric directional Josephson devices, PRX Quantum **2**, 040360 (2021).

[12] C. Macklin, K. O'Brien, D. Hover, M. E. Schwartz, V. Bolkhovsky, X. Zhang, W. D. Oliver, and I. Siddiqi, A

near–quantum-limited Josephson traveling-wave parametric amplifier, Science **350**, 307 (2015).
[13] A. Zorin, Flux-driven Josephson traveling-wave parametric amplifier, Phys. Rev. Appl. **12**, 044051 (2019).
[14] K. Peng, M. Naghiloo, J. Wang, G. D. Cunningham, Y. Ye, and K. P. O'Brien, Floquet-mode traveling-wave parametric amplifiers, PRX Quantum **3**, 020306 (2022).
[15] B. Ho Eom, P. K. Day, H. G. LeDuc, and J. Zmuidzinas, A wideband, low-noise superconducting amplifier with high dynamic range, Nat. Phys. **8**, 623 (2012).
[16] M. Malnou, M. Vissers, J. Wheeler, J. Aumentado, J. Hubmayr, J. Ullom, and J. Gao, Three-wave mixing kinetic inductance traveling-wave amplifier with near-quantum-limited noise performance, PRX Quantum **2**, 010302 (2021).
[17] J. Heinsoo, C. K. Andersen, A. Remm, S. Krinner, T. Walter, Y. Salathé, S. Gasparinetti, J.-C. Besse, A. Potočnik, A. Wallraff, and C. Eichler, Rapid high-fidelity multiplexed readout of superconducting qubits, Phys. Rev. Appl. **10**, 034040 (2018).
[18] R. Kaufman and O. Naaman, Parametric amplifier matching using Legendre prototypes, ArXiv:2303.00184 (2023).
[19] T. White, *et al.*, Readout of a quantum processor with high dynamic range Josephson parametric amplifiers, Appl. Phys. Lett. **122**, 014001 (2023).
[20] C. Eichler and A. Wallraff, Controlling the dynamic range of a Josephson parametric amplifier, EPJ Quantum Technol. **1**, 1 (2014).
[21] L. Planat, R. Dassonneville, J. P. Martínez, F. Foroughi, O. Buisson, W. Hasch-Guichard, C. Naud, R. Vijay, K. Murch, and N. Roch, Understanding the saturation power of Josephson parametric amplifiers made from SQUID arrays, Phys. Rev. Appl. **11**, 034014 (2019).
[22] J. Y. Mutus, T. C. White, R. Barends, Y. Chen, Z. Chen, B. Chiaro, A. Dunsworth, E. Jeffrey, J. Kelly, A. Megrant, C. Neill, P. J. J. O'Malley, P. Roushan, D. Sank, A. Vainsencher, J. Wenner, K. M. Sundqvist, A. N. Cleland, and J. M. Martinis, Strong environmental coupling in a Josephson parametric amplifier, Appl. Phys. Lett. **104**, 263513 (2014).
[23] K. Huang, Q. Guo, C. Song, Y. Zheng, H. Deng, Y. Wu, Y. Jin, X. Zhu, and D. Zheng, Fabrication and characterization of ultra-low noise narrow and wide band Josephson parametric amplifiers, Chin. Phys. B **26**, 094203 (2017).
[24] Y.-P. Lu, Q. Zuo, J.-Z. Pan, J.-L. Jiang, X.-Y. Wei, Z.-S. Li, W.-Q. Xu, K.-X. Zhang, T.-T. Guo, S. Wang, C.-H. Cao, W.-W. Xu, G.-Z. Sun, and P.-H. Wu, An easily-prepared impedance matched Josephson parametric amplifier, Chin. Phys. B **30**, 068504 (2021).
[25] Y. Lu, W. Xu, Q. Zuo, J. Pan, X. Wei, J. Jiang, Z. Li, K. Zhang, T. Guo, S. Wang, C. Cao, H. Wang, W. Xu, G. Sun, and P. Wu, Broadband Josephson parametric amplifier using lumped-element transmission line impedance matching architecture, Appl. Phys. Lett. **120**, 082601 (2022).
[26] T. Roy, S. Kundu, M. Chand, A. M. Vadiraj, A. Ranadive, N. Nehra, M. P. Patankar, J. Aumentado, A. A. Clerk, and R. Vijay, Broadband parametric amplification with impedance engineering: Beyond the gain-bandwidth product, Appl. Phys. Lett. **107**, 262601 (2015).
[27] J. Grebel, A. Bienfait, É. Dumur, H.-S. Chang, M.-H. Chou, C. R. Conner, G. A. Peairs, R. G. Povey, Y. P. Zhong, and A. N. Cleland, Flux-pumped impedance-engineered broadband Josephson parametric amplifier, Appl. Phys. Lett. **118**, 142601 (2021).
[28] P. Duan, Z. Jia, C. Zhang, L. Du, H. Tao, X. Yang, L. Guo, Y. Chen, H. Zhang, Z. Peng, W. Kong, H.-O. Li, G. Cao, and G.-P. Guo, Broadband flux-pumped Josephson parametric amplifier with an on-chip coplanar waveguide impedance transformer, Appl. Phys. Express **14**, 042011 (2021).
[29] D. Ezenkova, D. Moskalev, N. Smirnov, A. Ivanov, A. Matanin, V. Polozov, V. Echeistov, E. Malevannaya, A. Samoylov, E. Zikiy, and I. Rodionov, Broadband SNAIL parametric amplifier with microstrip impedance transformer, Appl. Phys. Lett. **121**, 232601 (2022).
[30] S. Wu, D. Zhang, R. Wang, Y. Liu, S.-P. Wang, Q. Liu, J. S. Tsai, and T. Li, Vacuum-gap-based lumped element Josephson parametric amplifier, Chin. Phys. B **31**, 010306 (2022).
[31] O. Naaman and J. Aumentado, Synthesis of parametrically coupled networks, PRX Quantum **3**, 020201 (2022).
[32] O. Naaman, J. A. Strong, D. G. Ferguson, J. Egan, N. Bailey, and R. T. Hinkey, Josephson junction microwave modulators for qubit control, J. Appl. Phys. **121**, 073904 (2017).
[33] O. Naaman, D. G. Ferguson, A. Marakov, M. Khalil, W. F. Koehl, and R. J. Epstein, in *2019 IEEE MTT-S International Microwave Symposium (IMS)* (IEEE, Boston, MA, USA, 2019), p. 259.
[34] G. Matthaei, A study of the optimum design of wideband parametric amplifiers and up-converters, IRE Trans. Microw. Theory Tech. **9**, 23 (1961).
[35] W. Getsinger, Prototypes for use in broadbanding reflection amplifiers, IEEE Trans. Microw. Theory Tech. **11**, 486 (1963).
[36] W. Getsinger and G. Matthaei, Some aspects of the design of wide-band up-converters and nondegenerate parametric amplifiers, IEEE Trans. Microw. Theory Tech. **12**, 77 (1964).
[37] R. Kaufman, T. White, M. I. Dykman, A. Iorio, G. Stirling, S. Hong, A. Opremcak, A. Bengtsson, L. Faoro, J. C. Bardin, T. Burger, R. Gasca, and O. Naaman, Josephson parametric amplifier with Chebyshev gain profile and high saturation, ArXiv:2305.17816 (2023).
[38] P. H. Smith, Transmission line calculator, Electronics **12**, 29 (1939).
[39] J. F. White, *High Frequency Techniques: An Introduction to RF and Microwave Engineering* (IEEE Press, Wiley-Interscience, Hoboken, NJ, 2004).
[40] K. M. Sundqvist, S. Kintaş, M. Simoen, P. Krantz, M. Sandberg, C. M. Wilson, and P. Delsing, The pumpistor: A linearized model of a flux-pumped superconducting quantum interference device for use as a negative-resistance parametric amplifier, Appl. Phys. Lett. **103**, 102603 (2013).
[41] K. M. Sundqvist and P. Delsing, Negative-resistance models for parametrically flux-pumped superconducting quantum interference devices, EPJ Quantum Technol. **1**, 6 (2014).

[42] K. He, G. Dai, Q. Yu, Y. He, C. Zhao, J. Liu, and W. Chen, Simulation of a flux-pumped Josephson parametric amplifier with a detailed SQUID model using the harmonic balance method, Supercond. Sci. Technol. **36**, 045010 (2023).
[43] N. Zobrist, B. H. Eom, P. Day, B. A. Mazin, S. R. Meeker, B. Bumble, H. G. LeDuc, G. Coiffard, P. Szypryt, N. Fruitwala, I. Lipartito, and C. Bockstiegel, Wide-band parametric amplifier readout and resolution of optical microwave kinetic inductance detectors, Appl. Phys. Lett. **115**, 042601 (2019).
[44] D. M. Pozar, *Microwave Engineering* (Wiley, Hoboken, NJ, 2012), 4th ed.
[45] R. E. Collin, *Foundations for Microwave Engineering*, 2nd ed.IEEE Press Series on Electromagnetic Wave Theory (IEEE Press, New York, 2001),
[46] J. M. Manley and H. E. Rowe, Some general properties of nonlinear elements-part I. General energy relations, Proc. IRE **44**, 904 (1956).
[47] SimSmith, http://www.ae6ty.com/Smith_Charts.html.
[48] Smith, http://www.fritz.dellsperger.net/smith.html.
[49] R. Rhea, The yin-yang of matching: Part 1—Basic matching concepts, High Frequency Electronics **5**, 16 (2006).
[50] R. Rhea, The yin-yang of matching: Part 2—–Practical matching techniques, High Frequency Electronics **5**, 28 (2006).
[51] M. Hatridge, R. Vijay, D. H. Slichter, J. Clarke, and I. Siddiqi, Dispersive magnetometry with a quantum limited SQUID parametric amplifier, Phys. Rev. B **83**, 134501 (2011).
[52] A. T. Baust, Ph.D. thesis, Technische Universitat München (2010).
[53] L. Ranzani and J. Aumentado, Graph-based analysis of nonreciprocity in coupled-mode systems, New J. Phys. **17**, 023024 (2015).
[54] M. O. Scully and M. S. Zubairy, *Quantum Optics* (Cambridge University Press, Cambridge, New York, 1997).